



MUNDFAB 

This project has received funding from the European Union's Horizon 2020 research and innovation programme under grant agreement No 871813.

ICT Project No 871813
MUNDFAB
Modeling Unconventional Nanoscaled
Device FABrication

**D4.6: Final experimental results on laser
annealing**

R. Daubriac¹, R. Demoulin¹, J. Muller¹, F. Cristiano¹, G. Larrieu¹, M. Opprecht², S. Kerdiles², J.-M. Hartmann², P. P. Michałowski³, A. La Magna⁴, D. Ricciarelli⁴

¹ LAAS-CNRS, Université de Toulouse, 31400 Toulouse, France

² Université Grenoble Alpes, CEA-LETI, 38000 Grenoble, France

³ Łukasiewicz Research Network, Institute of Microelectronics and Photonics, 02-668 Warsaw, Poland

⁴ CNR-IMM, 95121 Catania Italy

09/01/2023



Quality management

This deliverable was reviewed by:

Ioannis Deretzis (Researcher at CNR-IMM Catania)

Tibor Grasser (Professor at TU Wien)

Contents

Abstract.....	3
Introduction	4
1. Evolution of the Liquid/Solid Interface Roughness in $\text{Si}_{1-x}\text{Ge}_x$ Layers Processed by Nanosecond Laser Annealing.....	5
1.1. Elaboration and processing of $\text{Si}_{1-x}\text{Ge}_x$ layers	5
1.2. Quantification of the l/s interface roughness.....	6
1.3. Measurement of l/s interface roughness in undoped $\text{Si}_{1-x}\text{Ge}_x$ layers.....	6
1.4. Effect of B-doping on $\text{Si}_{1-x}\text{Ge}_x$ laser annealed layers	8
1.5. Evolution of l/s interface in r- $\text{Si}_{1-x}\text{Ge}_x$ layer	10
1.6. Key information	11
2. Ge evolution and surface structuration in relaxed SiGe	12
2.1. Ge segregation in r- $\text{Si}_{1-x}\text{Ge}_x$	12
2.2. Surface structuration of r- $\text{Si}_{1-x}\text{Ge}_x$	12
2.3. Key information	14
3. Investigation of laser annealing on patterned $\text{Si}_{1-x}\text{Ge}_x$ structures.....	15
3.1. Optimization of vertical patterning processes for SiGe substrates.....	15
3.1.1. Characterization of bulk substrates.....	15
3.1.2. Surface nanopatterning by e-beam lithography	16
3.1.3. Vertical etching of SiGe nanostructures.....	17
3.2. Fabrication of periodic nanostructures for laser annealing studies	19
3.2.1. Laser annealing of SiGe/SiO ₂ interface.....	19
3.2.2. Test fabrication of dense nanobeam arrays on relaxed SiGe.....	19
3.2.3. Sample fabrication for laser anneal studies	21
3.3. Key information	24
4. Dopant activation in laser annealed strained SiGe layers	25
4.1. Experimental details and characterization techniques	25
4.1.1. Fabrication process and laser annealing conditions.....	25
4.1.2. Characterization and analysis methods	25

4.1.3. Activation analysis method	26
4.2. Structural investigation boron-doped Si _{1-x} Ge _x layers upon NLA.....	27
4.2.1. Laser regimes identification	27
4.2.2. Strain relaxation phenomenon and energy density	28
4.2.3. Strain recovery threshold difference due to doping	29
4.3. Electrical properties of Si _{0.7} Ge _{0.3} :B layers annealed by NLA (CEA)	30
4.3.1. Activation in Si _{0.7} Ge _{0.3} as-grown layers	30
4.3.2. Sheet resistance variations with energy density	32
4.3.3. Activation calculation	34
4.4. Preliminary results on Si _{0.7} Ge _{0.3} :B layers annealed by NLA (C2N)	36
4.4.1. Experimental details	36
4.4.2. Preliminary discussion on electrical measurements.....	36
4.5. Key information	40
Conclusion	41
References.....	43

Abstract

This deliverable reports on the final rounds of experiments on undoped and boron-doped strained and relaxed SiGe thin layers annealed by laser. Structural, chemical and electrical properties have been studied on these layers thanks to many characterization techniques such as TEM, AFM, SIMS and Hall Effect. Based on the conclusions made on the previous experimental studies, the understanding of the different phenomena has been refined. Concerning the evolution of the liquid/solid interface roughness in strained SiGe layers, it strongly depends on the initial Ge content but also on the strain state of the layer. When considering relaxed layers, the roughness remains highly impacted by the Ge content, and so, very likely by the first stages of the melt regime. In the case of boron-doped strained SiGe layers, the evolution of the activation must take into account the crystal quality and the strain state of the layer depending on the energy density. Doing so, the results suggest an improvement of the global activation, similarly to conventional cases described in the literature. Also, in the aim of large-scale integration, a process for the fabrication of 3D nanostructures has been optimized on provided SiGe sheet layers in order to study the impact of nanosecond laser annealing on such small structures, in terms of structure conservation and dopant activation. Finally, in addition to these conclusions, future designs of experiments to pursue these investigations are provided along with new possible angle of analysis.

Introduction

This deliverable gives a report on the results from the final rounds of experiments on undoped and/or boron-doped strained and/or relaxed SiGe thin layers annealed by nanosecond laser annealing (NLA). Most topics approached in this document are an extension of the questions raised in deliverable 4.3, previously released. This report is divided in four sections, related to structural investigations (1-3) and dopant activation (4).

In the first section, the evolution of the liquid/solid (l/s) interface roughness of undoped SiGe layers annealed by NLA is studied thanks to structural and chemical characterizations (mainly TEM, AFM, and SIMS). Strained and relaxed layers have been investigated to highlight the link between the strain state, the Ge content and the l/s interface roughness, depending on the laser conditions. The second section focuses principally on the Ge redistribution and surface structuration of laser-annealed relaxed SiGe layers with different initial Ge content. The specific case of relaxed SiGe layers allows examining, similarly to Section 1, the dominant levers leading to structural modifications but excluding the compressive strain variable. In the third section, the optimizations made on the fabrication process of vertical 1D nanostructures (nanowires and nanolines) starting from relaxed SiGe layers of different Ge content are presented. A particular attention has been dedicated to surface preparation, reactive ion etching (RIE) etching conditions and dimension limitations concerning nanostructures arrays fabrication. Finally, a refined understanding on the evolution of the boron activation in laser-annealed strained SiGe layers is proposed. Also, electrical measurements, concurrently to structural analysis, are retroactively used to further examine electrical properties variations with laser energy density. As well, preliminary results on the impact of pulse duration on structural and electrical properties are presented.

For each section, a specific set of samples has been used. For this reason and for the sake of analysis clarity, a dedicated description of the samples characteristics is provided at the beginning of each investigation. Moreover, each section includes a concise summary of the key information. A subsequent and general conclusion is formulated at the end of the report, putting possible future investigations into perspective.

1. Evolution of the Liquid/Solid Interface Roughness in $\text{Si}_{1-x}\text{Ge}_x$ Layers Processed by Nanosecond Laser Annealing

1.1. Elaboration and processing of $\text{Si}_{1-x}\text{Ge}_x$ layers

Three different series of $\text{Si}_{1-x}\text{Ge}_x$ layers have been investigated in this work. All the samples have been elaborated at CEA-LETI. Characteristics of the analysed samples are reported in **Table 1.1**.

Undoped and B-doped 30 nm-thick strained $\text{Si}_{1-x}\text{Ge}_x$ layers ($x = 0.1 - 0.4$) were grown on 300 mm n-type Si (001) wafers at 550°C by Reduced Pressure Chemical Vapor Deposition (RPCVD) in an Epsilon 3200 tool from ASM. They are referred to as s-SiGe and s-SiGe:B. Before the deposition, an hydrofluoric acid wet cleaning followed by an in-situ H_2 bake at 1100°C were performed on Si surfaces. For s-SiGe layers, GeH_4 and Si_2H_6 were used as Ge and Si precursors, respectively. For s-SiGe:B layers, SiH_2Cl_2 and B_2H_6 were used as precursors for Si and B, respectively. In this case, the $\text{Si}_{1-x}\text{Ge}_x$ growth was preceded by a 100-nm n-type doped Si layer to form a p-n junction. Three levels of doping have been considered, at 7.4×10^{19} , 1.4×10^{20} and 2.3×10^{20} B atoms. cm^{-3} (as measured by SIMS).

Fully relaxed $\text{Si}_{1-x}\text{Ge}_x$ layers ($x = 0.2$ and 0.5) were grown on 200 mm p-type Si (001) substrates. These layers are referred to as r-SiGe. Fabrication of r-SiGe was carried out by RPCVD, in an Epi Centura 5200 tool, following a two steps process: (i) a deposition of a SiGe layer with linearly graded Ge concentration, with a 10%. μm^{-1} ramp used to reach the targeted Ge concentration, followed by (ii) a deposition of about one micron thick $\text{Si}_{0.8}\text{Ge}_{0.2}$ or $\text{Si}_{0.5}\text{Ge}_{0.5}$ layers. They were grown at 850-900°C in order to minimize the threading dislocation density, resulting in the formation of strain-free μm -thick r-SiGe layer on top. Finally, Chemical Mechanical Polishing was performed on both layers to remove the surface cross-hatch patterns usually formed during the process.

All three series of SiGe layers were annealed by UltraViolet Nanosecond Laser Annealing (UV-NLA). This was performed using a SCREEN-LT3100 system based on a XeCl excimer laser with a 308 nm wavelength and a pulse duration of 146 ns or 160 ns. The range of laser energy density were chosen to investigate the evolution of SiGe layers in its melt regimes.

Series	Ge content (%)	Thickness (nm)	Doping (cm^{-3})	Energy density range (J/cm^2)	Laser Pulse FWHM (ns)
s-SiGe	10	30	-	1.51 – 2.48	146
	20	30	-	1.40 – 2.38	146
	30	30	-	1.31 – 2.28	146
	40	30	-	1.21 – 2.18	146
s-SiGe:B	30	30	(A) 7.4×10^{19}	1.21 – 2.42	160
	30	30	(B) 1.4×10^{20}	1.21 – 2.41	160
	30	30	(C) 2.3×10^{20}	1.20 – 2.40	160
r-SiGe	20	1000+2000	-	0.3 – 2.50	160
	50	1000+5000	-	0.3 – 2.50	160

Table 1.1: Characteristics of the $\text{Si}_{1-x}\text{Ge}_x$ layers.

1.2. Quantification of the I/s interface roughness

The contrast observed on STEM-HAADF micrographs is directly related to the chemical composition. This allows to differentiate the phases in laser annealed SiGe layers. **Fig. 1.1(a,b)** represent two STEM-HAADF micrographs recorded in 30 nm-thick s-SiGe layers annealed by UV-NLA. In STEM-HAADF mode, the redistribution of Ge is marked by a contrast gradient in the annealed area. This imaging technique also allows to evidence the position and the shape of the I/s interface, which corresponds to the limit between the melted and the unmelted areas. In these micrographs, at each x-coordinate an intensity threshold (along the z-axis) is determined to extract the depth (y-position) of the I/s interface. In the partial melt regime this threshold corresponds to the mid-level between the lowest intensity of melted area and the highest intensity of unmelted area. The same procedure is used for the full melt regime criterium (but with inversed contrast levels). Once the I/s interface is entirely reconstructed, the roughness R of the interface can be estimated following equation (1.1):

$$R = \frac{1}{N} \sum_{i=1}^n |y_i - d_{I/s}| \quad (1.1)$$

The mean depth of the I/s interface is represented by $d_{I/s}$ while its depth at the position i is given by the coordinate y_i . N corresponds to the total number of measurements (i.e number of pixels in x-axis). Here, R represents the mean variation of the I/s interface around its mean depth. Two examples of roughness measurement are shown in **Fig. 1.1**. The roughness of I/s interfaces have been estimated at 1.23 ± 0.15 nm (**Fig. 1.1(a)**, considered as “rough”) and 0.54 ± 0.09 nm (**Fig. 1.1(b)**, considered as “flat”), respectively.

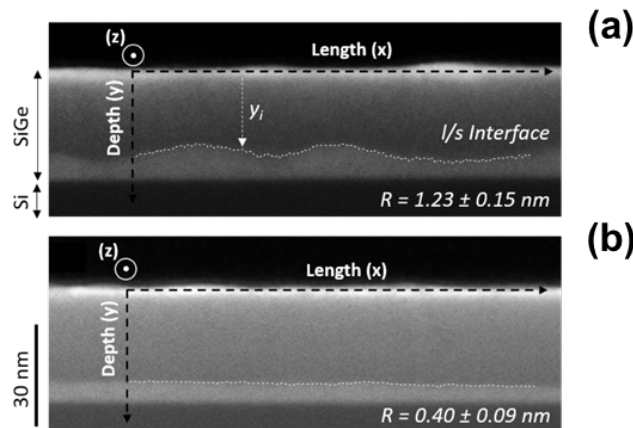


Figure 1.1: STEM-HAADF micrographs of 30 nm-thick s-SiGe layers. Both micrographs have been overlaid with the representative curve of the I/s interface. Z-axis corresponds to the intensity. (a) and (b) represent an example of a rough and a flat interface, respectively.

1.3. Measurement of I/s interface roughness in undoped Si_{1-x}Ge_x layers

The procedure stated right before has been used in order to quantify the evolution of the I/s interface roughness as a function of the elaboration parameters and processing method. For each undoped s-Si_{1-x}Ge_x series, the I/s interface roughness has been computed for

different laser energy densities leading to the partial or full melt of the SiGe layer. The results have been represented in the **Fig. 1.2** as a function of the mean melt depth.

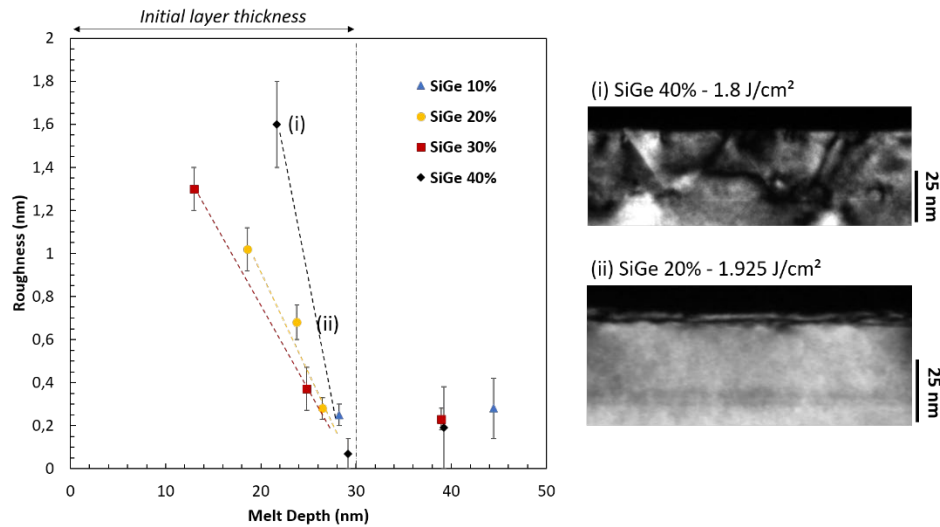


Figure 1.2: Evolution of the I/s interface roughness as a function of the melt depth in undoped s-SiGe layers for different Ge composition. (i) and (ii) shows DF-TEM micrographs of $\text{Si}_{0.6}\text{Ge}_{0.4}$ annealed at 1.8 J/cm^2 and $\text{Si}_{0.6}\text{Ge}_{0.4}$ annealed at 1.925 J/cm^2 , respectively.

For samples containing 20 to 40% of Ge, a clear trend can be observed. On one side, for a melt depth near or higher than the initial thickness of the s-SiGe layer (i.e. 30 nm), the measured roughness values are stabilized around 0.2 nm independently of the Ge content. On the other side, in the partial melt regime, i.e. for melt depth lower than 30 nm, the roughness parameter is always higher. As evidenced by the dashed lines (**Fig. 1.2**) the I/s interface roughness tends to decrease when the melt depth approaches the transition from partial to full melt. Here, at the proximity of the SiGe/Si interface, the flattening of the I/s interface may be explained by the difference of the melting temperature between Si (1412°C) and Ge (938°C). The melting temperature of the SiGe alloy is lower than the one of the Si substrate. Then, even in the presence of a rougher I/s interface in the partial melt regime, the SiGe layer must be completely melted even before the Si substrate starts to melt, leading to the formation of a flat interface at the transition from the partial to full melt regime. To confirm this hypothesis, another experiment has been made in 45 nm-thick s- $\text{Si}_{0.7}\text{Ge}_{0.3}$ layer (not shown here). In this case, at a higher melt depth (around 35 nm) we still observed a rough I/s interface with a roughness parameter R of 2.0 nm. This demonstrates that the flattening observed in 30 nm-thick SiGe is mainly linked to the proximity of the I/s interface and not to the melt depth. It must be noted that the difference of roughness observed between 45 and 30 nm-thick s- $\text{Si}_{0.7}\text{Ge}_{0.3}$ layer may be explained in part by the higher elastic energy stored in the 45 nm-thick SiGe layer.

While the roughness evolution measured for a Ge content of 20 and 30% is almost similar, **Fig. 1.2** highlights an increase of the I/s interface roughness for a Ge content of 40%. The increase of the I/s interface roughness in relation with an increase of Ge content may be linked to the higher elastic energy stored in the $\text{Si}_{0.6}\text{Ge}_{0.4}$ layer or to the initial nano-structuration during the surface melt. On this second point, the structures observed at the melt onset in s- $\text{Si}_{0.8}\text{Ge}_{0.2}$ and s- $\text{Si}_{0.6}\text{Ge}_{0.4}$ are displayed on **Fig. 1.3**. In both cases, these AFM scans reveal the presence of cross-shaped islands extended in the $\langle 100 \rangle$ directions at the surface of the s-

SiGe layer. The nano-structuration observed in $\text{Si}_{0.6}\text{Ge}_{0.4}$ may result in a higher density of smaller surface islands with a deeper melt depth leading to an increase of the l/s interface roughness at the surface to partial melt transition. Cross-sections taken in DF-TEM mode are presented in the **Fig. 1.2**. These micrographs highlight the presence of defects in s- $\text{Si}_{0.6}\text{Ge}_{0.4}$ laser annealed layers at 1.8 J/cm^2 while s- $\text{Si}_{0.8}\text{Ge}_{0.2}$ laser annealed layers at 1.925 J/cm^2 remain defects-free. These DF-TEM micrographs allow to evidence that, at a similar melt depth, such an increase of the l/s interface roughness may favour the relaxation of the strained layer with the formation of strain relieving defects.

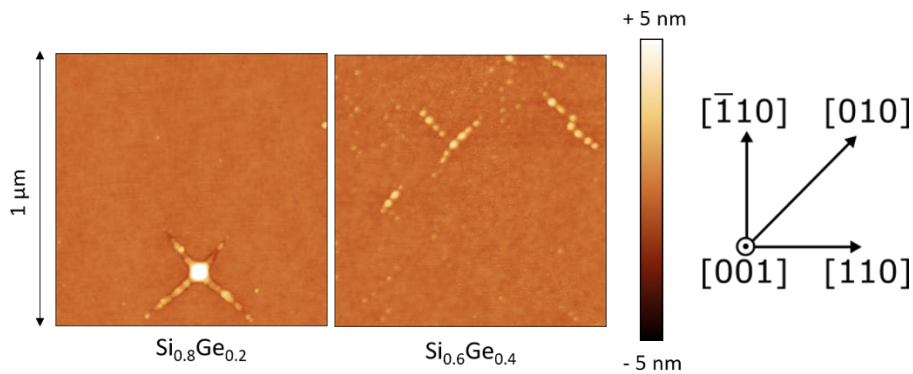


Figure 1.3: $1 \times 1 \mu\text{m}^2$ AFM scans after laser annealing of $\text{Si}_{0.8}\text{Ge}_{0.2}$ at 1.55 J/cm^2 and $\text{Si}_{0.6}\text{Ge}_{0.4}$ at 1.32 J/cm^2 . These laser energy densities correspond to the energy required to reach the melt onset.

Concerning the origin of the l/s interface roughness in the partial melt regime, several phenomena can be involved. In fact, this may be induced (i) by the impact of the Ge content on the initial strain state of the layer or by (ii) the influence of the Ge content on the surface nano-structuration observed during the surface melt regime. Besides, both of these phenomena may interact with each other. To determine the origin of the roughness of the l/s interface and its influence on the layer characteristics, these effects must be decorrelated. For that purpose, the effect of the initial strain on the l/s interface roughness have been investigated in two ways: (i) by reducing the initial strain by B-doping and (ii) by removing the strain and analyzing r-SiGe layers. The two following parts will describe these investigations.

1.4. Effect of B-doping on $\text{Si}_{1-x}\text{Ge}_x$ laser annealed layers

Due to the smaller size of the B atoms, the introduction of B in the SiGe crystal lattice should result in a reduction of the B-doped SiGe layer lattice parameter compared to the undoped one. As a result, this kind of doping is expected to result in a decrease of the initial strain state of the $\text{Si}_{1-x}\text{Ge}_x$ layer. As mentioned in Section 1.1, three different levels of B-doping referred to as low, medium and high have been performed in s- $\text{Si}_{0.7}\text{Ge}_{0.3}$ layers. Working on B-doped samples with a fixed Ge content allows to reduce the initial strain of the $\text{Si}_{1-x}\text{Ge}_x$ layer without interacting with the surface nano-structuration.

In s-SiGe:B layers, the B-doping has no influence on the laser annealing process and all the different melt regimes are triggered at the same energy densities for undoped as well as B-doped s- $\text{Si}_{0.7}\text{Ge}_{0.3}$ layers: the melt and partial melt threshold are observed at 1.45 J/cm^2 and 1.78 J/cm^2 , respectively. **Fig. 1.4** shows the mean melt depth of the l/s interface for the different levels of B-doping for s- $\text{Si}_{0.7}\text{Ge}_{0.3}$ layers at the transition between the surface and the

partial melt regime. For each of them, the corresponding SEM observation of the surface has been added. This clearly demonstrates that the mean melt depth (around 18 nm) as well as the nano-structuration of the surface are not affected by the B-doping level.

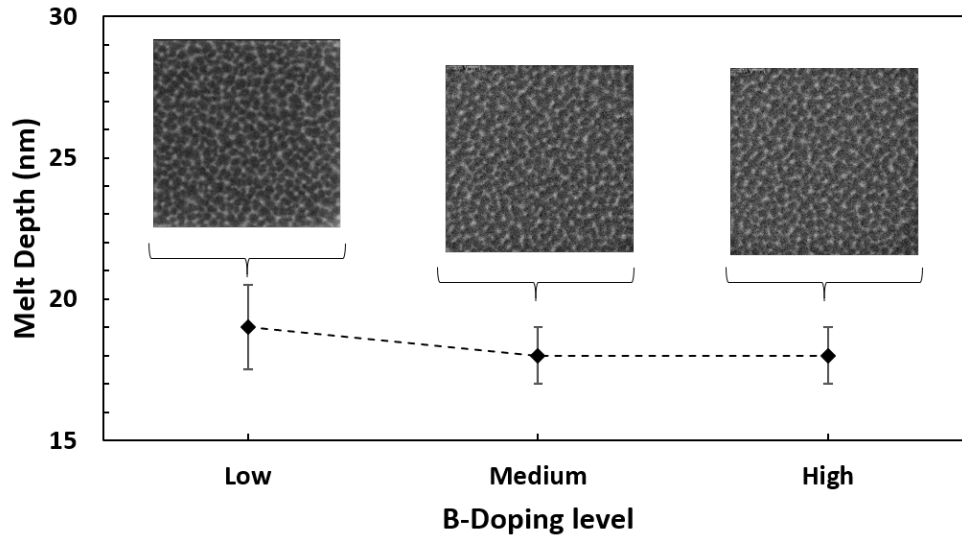


Figure 1.4: Melt depth measured at the surface to partial melt transition as a function of the B-doping level in $s\text{-Si}_{0.7}\text{Ge}_{0.3}$: B. SEM micrographs of the sample surface have been added for each one. The scale is $1 \times 1 \mu\text{m}^2$.

Figs. 1.5(a) and 1.5(b) display two STEM-HAADF micrographs of low and high B-doped $s\text{-Si}_{0.7}\text{Ge}_{0.3}$ layers laser annealed at 1.95 J/cm^2 . In both cases, the melt depth can be estimated at 27 nm. If no differences have been observed concerning the nano-structuration of the surface or the melt depth, these micrographs taken in cross section qualitatively show a difference in the roughness of the I/s interface. These roughness values have been quantitatively estimated as a function of the B-doping level for layers annealed at 1.95 J/cm^2 . The results are represented in **Fig. 1.5(c)**. By increasing the B-doping level, the R parameter decreases until it reaches its minimum for the high B-doped case resulting in a significant flattening of the I/s interface induced by B-doping. This suggests that a decrease of the initial strain state allows decreasing the roughness of the I/s interface. On the same graph (**Fig. 1.5(c)**), the evolution of the degree of relaxation as a function of the B-doping level has been superimposed with the roughness evolution. The degree of relaxation of these $s\text{-Si}_{0.7}\text{Ge}_{0.3}$ layers has been extracted from Reciprocal Space Maps performed by HR-XRD. For medium and high doped samples, which present smoother I/s interfaces ($R < 0.6 \text{ nm}$), the $\text{Si}_{0.7}\text{Ge}_{0.3}$ layer remains perfectly strained. However, for low doped $\text{Si}_{0.7}\text{Ge}_{0.3}$ layer, the R parameter is larger ($R = 1.2 \text{ nm}$) and a degree of relaxation of 25% is observed. As in the undoped case, these observations confirm that a rough I/s interface induces the relaxation of the $\text{Si}_{1-x}\text{Ge}_x$ layers. From these experiments it can be clearly observed that the reduction of the initial strain state of $s\text{-Si}_{0.7}\text{Ge}_{0.3}$ layers induced by B-doping leads to a flattening of the I/s interface in the melt regime. Moreover, it also indicates that a strong correlation between the I/s interface roughness and the layer crystallinity exists.

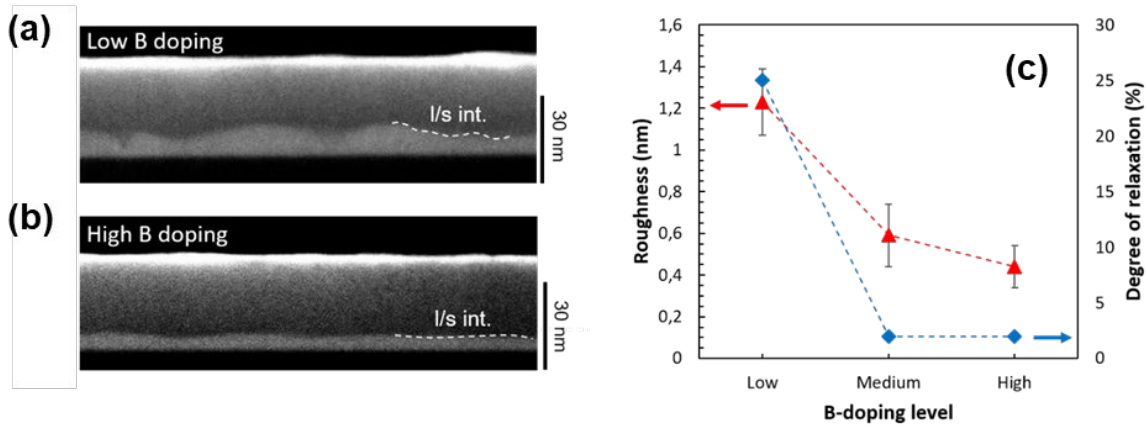


Figure 1.5: (a) and (b) represent STEM-HAADF micrographs taken in cross section of $s\text{-Si}_{0.7}\text{Ge}_{0.3}$ B layers annealed at 1.95 J/cm^2 . (c) Evolution of the I/s interface roughness (red dashed line) and of the degree of relaxation (blue dashed line) as a function of the B-doping level.

1.5. Evolution of the I/s interface in the r- $\text{Si}_{1-x}\text{Ge}_x$ layer

To analyze the contribution of the strain state on the I/s interface roughness the second method consists in completely removing the initial strain state of the SiGe layer. For that, two series of fully relaxed $\text{Si}_{1-x}\text{Ge}_x$ layers (with $x = 0.2$ and 0.5) have been investigated.

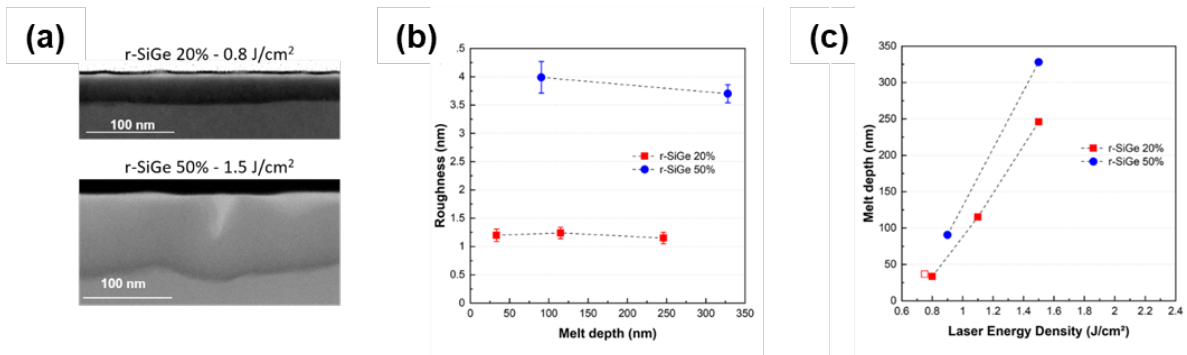


Figure 1.6: (a) Evolution of the melt depth as a function of the laser energy density in r-SiGe layers. The empty symbol corresponds to the maximum melt depth measured in surface melt regime. (b) Example of STEM-HAADF micrographs demonstrating the difference of roughness measured between r- $\text{Si}_{0.8}\text{Ge}_{0.2}$ and s- $\text{Si}_{0.5}\text{Ge}_{0.5}$. (c) Evolution of the I/s interface roughness as a function of the melt depth in r-SiGe layers.

Fig. 1.6(a) shows two cross sections observed in the STEM-HAADF mode recorded on r- $\text{Si}_{0.8}\text{Ge}_{0.2}$ and r- $\text{Si}_{0.5}\text{Ge}_{0.5}$ layers annealed in the same range of energy densities (0.8 and 0.9 J/cm^2 , respectively). First, we discuss the laser energy densities required to reach the different melt regimes. In fact, in a strained layer these energy densities are quite higher, for instance, the melt onset is reached at 1.3 J/cm^2 in s- $\text{Si}_{0.6}\text{Ge}_{0.4}$. This may be linked to a difference of the heat conductivity and the refraction index that can be induced by the crystallinity of the layer (relaxed or strained) and/or by the thickness of the SiGe layer. These

micrographs also highlight a significant difference of melt depth and interface roughness. In these cases, the roughness parameter has been estimated at 1.2 nm in r-Si_{0.8}Ge_{0.2} and 4 nm in r-Si_{0.5}Ge_{0.5}. For both cases, the evolution of the roughness as a function of the melt depth has been represented in **Fig. 1.6(b)**. This graph shows that the roughness remains almost constant regardless of the melt depth for both Ge contents. To explain the difference of roughness observed between layers with 20% and 50% of Ge content, attention has been paid to the melt depth. In fact, as stated before, in SiGe alloys, the difference of melting temperature between Si and Ge implies a decrease of the melting temperature when the Ge content increases. The evolution of the melt depth as a function of the laser energy density is displayed in **Fig 1.6(c)**. As shown here, at a fixed energy density, this always results in deeper melt depth in r-Si_{0.5}Ge_{0.5} compared to r-Si_{0.8}Ge_{0.2}. As a consequence, during the surface melt regime, a deeper melt in r-Si_{0.5}Ge_{0.5} may generate a higher l/s interface roughness at the transition from the surface melt regime to the partial melt regime.

1.6. Key information

Key information – Evolution of the l/s interface roughness in Si _{1-x} Ge _x layers	
1.1	Samples characteristics summary
1.2	Roughness can be quantified through <i>R</i> values (in nm) from STEM-HAADF micrographs
1.3	<ul style="list-style-type: none"> ➤ Flattening occurs when approaching SiGe/Si interface (full melt) ➤ In the partial melt regime, the roughness might primarily depend on the Ge content through (both amplified with increasing Ge content): <ul style="list-style-type: none"> • Initial strain • Surface structuration <p><u>To decorrelate both phenomena:</u> (1.4) Study of boron doping to modify initial strain (for a given Ge content) (1.5) Study of relaxed undoped SiGe layers</p>
1.4	3 different B-doping in 30 nm strained-Si _{0.7} Ge _{0.3} layers <ul style="list-style-type: none"> • Same conditions (melt depth, laser regime, surface structuration) • When B-doping decreases (initial strain increases), <i>R</i> decreases and: <ul style="list-style-type: none"> ▪ Low B-doping = partially relaxed layers with defects ▪ High B-doping = strained layers without defects <p>In initially strained SiGe layers, liquid/solid interface roughness is correlated to the crystalline quality of the layer (and so to the strain state)</p>
1.5	3 different B-doping in 30 nm strained-Si _{0.7} Ge _{0.3} layers <ul style="list-style-type: none"> • At a given Ge content, <i>R</i> is constant with <i>R</i>(20%Ge)=1.2 nm < <i>R</i>(50%Ge)=4.0 nm • But, at fixed energy density, melt depth(20%) < melt depth(50%) <p>In initially relaxed SiGe layers, liquid/solid interface roughness is correlated to the initial Ge content → to be confirmed using <i>R</i> quantification at the early stage of the partial melt regime for both Ge content</p>

2. Ge evolution and surface structuration in relaxed SiGe

2.1. Ge segregation in r-Si_{1-x}Ge_x

Fig. 2.1(a) to 2.1(c) show cross-sections taken in the STM-HAADF mode of r-Si_{0.8}Ge_{0.2} annealed at 0.75, 0.80 and 1.1 J/cm². Set apart the lower energy densities required for the different melt regimes, the melting process in r-SiGe follows the same steps as observed in s-SiGe layers [1]. In the present case, the surface melt regime occurs for laser energy densities ranging from 0.65 to 0.8 J/cm². In this range, surface islands progressively cover the entire layer surface until 0.8 J/cm², at which point a continuous layer is formed at the surface (**Fig. 2.1(b)**), evidencing the transition from the surface to the partial melt regime. It is interesting to note that from the first step of the partial melt, the melt depth (34 nm) already exceeds the thickness of s-SiGe layers. As for s-SiGe layers, a Z-contrast gradient can be observed on these STEM-HAADF micrographs. This contrast gradient highlights the redistribution of Ge towards the surface in the melted area. This Ge redistribution has been confirmed by the EDX profiles presented in **Fig. 2.1(d)** for each energy density. It can be noted that an increase of the laser energy density leads to an increase of the Ge composition at the layer surface, from 45% at 0.75 J/cm² to 75% at 1.1 J/cm². It must be added that for both r-Si_{0.8}Ge_{0.2} and r-Si_{0.5}Ge_{0.5} no defects are formed in the melted area even with a significant l/s interface roughness.

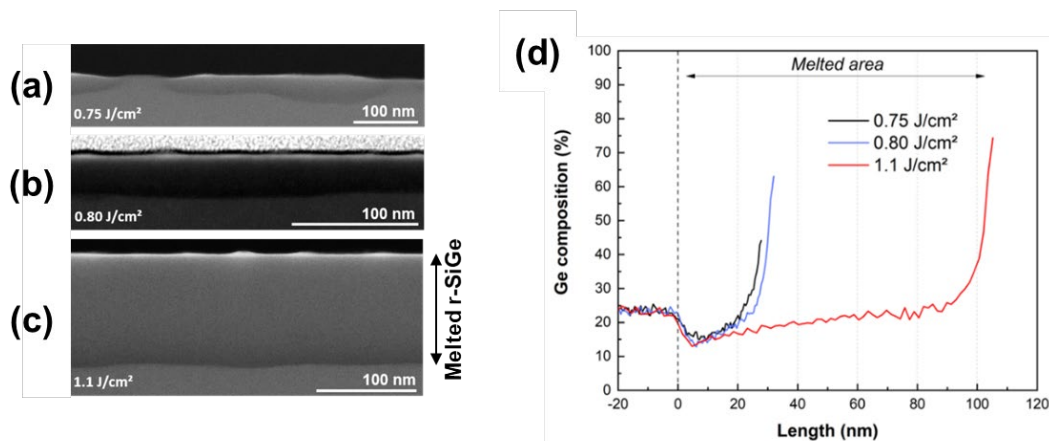


Figure 2.1: STEM-HAADF micrographs of r-Si_{0.8}Ge_{0.2} layers laser annealed at (a) 0.75 J/cm², (b) 0.80 J/cm² and (c) 1.1 J/cm². (d) Corresponding EDX profiles. The zero position corresponds to the position of the l/s interface.

2.2. Surface structuration of r-Si_{1-x}Ge_x

In r-SiGe layers, as shown in **Fig. 2.1**, until a melt depth of 110 nm no changes are observed in the Ge redistribution. However, at higher melt depth an abrupt modification of the layer structure and of the layer surface can be observed. **Fig. 2.2** represents the evolution of the surface structuration as a function of the laser energy density. It can be observed that, until 0.8 J/cm², the nano-structuration of the surface is almost similar to what can be observed for 30 nm-thick s-SiGe layers. The main difference is the formation of square-shaped islands instead of cross-shaped ones during the first steps (**Fig. 1.3**). Such square-shaped islands are usually observed in bulk Si or Ge layers. However, in the first step of the partial melt, i.e. at 0.8 J/cm², the surface structuration corresponds exactly to the one displayed in **Fig. 1.4** for s-Si_{0.7}Ge_{0.3}B. However, in the partial melt, the surface continues to evolve and a cellular

morphology is stabilized at higher energy densities. The cellular morphology is represented by a network of regular square shaped cells with an estimated dimension ranging from 110 to 180 nm (as seen on Fig. 2.2 for 1.5 J/cm²). This evolution is not specific to r-SiGe and such a cellular morphology has already been observed following the laser annealing of amorphous or strained SiGe layers [2-4]. Especially, it has been shown that the characteristics of the cellular morphology can be tuned by the layer thickness and the Ge composition [2].

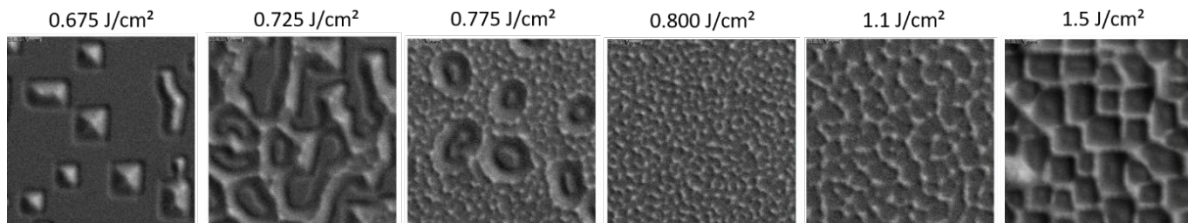


Figure 2.2: SEM micrographs of the surface of r-Si_{0.8}Ge_{0.2} layers for an increasing laser energy density. For all SEM micrographs, the scale is 1×1 μm².

Fig. 2.3(a) represents two cross-sections observed in the STEM-HAADF mode of r-Si_{0.8}Ge_{0.2} and r-Si_{0.5}Ge_{0.5} laser annealed at 1.5 J/cm². At this energy, both samples present a cellular morphology at their surface. In these micrographs, the bright contrasts show an important segregation of Ge that induces the formation of 80 and 325 nm-long pillars in the melted regions of r-SiGe layers. These pillars correspond to the walls observed in the cellular morphology at the layer surface. The composition of these pillars observed in TEM cross-sections (i.e. of the walls of the cellular morphology) has been estimated by EDX analysis. The EDX profile recorded through one of these walls in r-Si_{0.5}Ge_{0.5} is displayed in **Fig. 2.3(b)**. A Ge content of around 85% can be measured in the core of these walls. Moreover, a Ge content of almost 95% has been measured near to the surface of the layer (not shown here). Considering the thickness of the TEM lamella and the unregular disposition of the cells (**Fig. 2.1**), a superimposition of these Ge-rich walls with the surrounding Si_{1-x}Ge_x matrix may artificially reduce the real Ge composition during the EDX analysis. Actually, these walls may be considered to be composed of almost pure Ge.

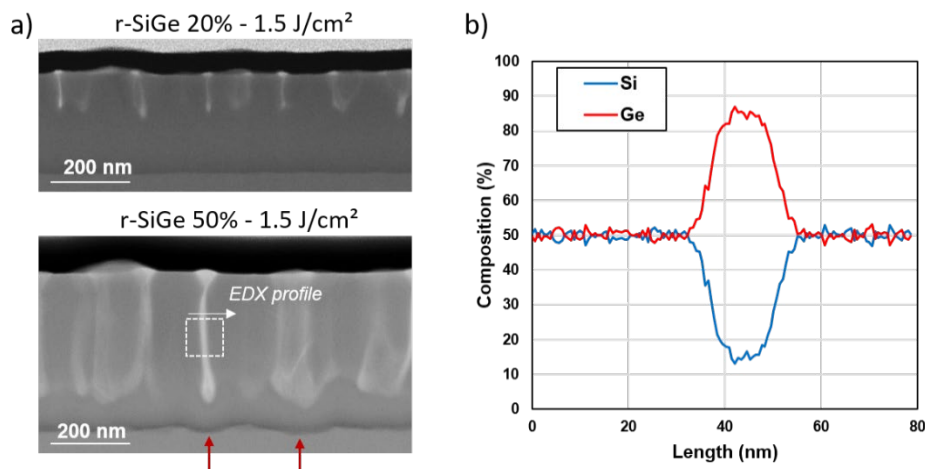


Figure 2.3: (a) STEM-HAADF micrographs taken in cross-section of s-Si_{1-x}Ge_x (x=0.2 and 0.5) layers laser annealed at 1.5 J/cm². (b) EDX composition profile recorded through the Ge-rich pillar.

A model for the formation of the cellular morphology in SiGe has been proposed in the literature, based on the analysis of a Cz-grown $\text{Si}_{0.85}\text{Ge}_{0.15}$ layer [2,5]. In these experiments, the l/s interface transforms from planar to faceted interface in the $\langle 110 \rangle$ direction. This faceting generates a lateral segregation of Ge and a growth of Ge-rich phases in the valleys, which tends to reduce the growth velocity at these locations. Then, the difference of growth velocity between Ge-rich and Ge-poor areas leads to the formation of Ge-rich walls up to the layer surface.

In the present case, whatever the Ge content, the l/s interface is clearly rough (Fig. 1.6(b)). During the first steps of the melt regime, from 0.75 to 1.1 J/cm², Ge segregates in the melted areas and the Ge composition at the layer surface continuously increases (Fig. 2.1(d)). This Ge segregation toward the surface may occur until localized Ge-rich phases are formed. The l/s interface roughness seems to have an important impact on the location of these Ge-rich phases which may trigger the formation of the walls. The STEM-HAADF micrograph of r- $\text{Si}_{0.5}\text{Ge}_{0.5}$ presented in the Fig. 2.3(a) clearly evidences that the Ge-rich walls must be only formed at specific location which corresponds to the valleys formed by the l/s interface (shown by red arrows). In this way, the roughness of the l/s interface will initiate the formation of Ge-rich phases. In the following steps, Ge will continue segregating laterally to form the walls and then the cellular morphology. Moreover, it must be noted that even if the exact mechanism occurring during the regrowth of the SiGe layer cannot be directly observed, the presence of $\langle 110 \rangle$ directed facets between the Ge-poor and Ge-rich phases near the surface (Fig. 2.2(a-d)) at the end of the regrowth presumes an evolution from an initially rough l/s interface to a faceted l/s interface.

2.3. Key information

Key information – Ge evolution and surface structuration in relaxed SiGe	
2.1	For relaxed SiGe layers annealed by NLA (20% and 50% Ge content): <ul style="list-style-type: none"> • Same laser regimes as in strained SiGe layers • Ge redistribution occurs • %Ge at surface increases with the energy density • No observable defects while <i>R</i> is high
2.2	Focusing on surface structuration: <ul style="list-style-type: none"> • For ED < 1.1 J/cm², same surface morphologies as observed in strained SiGe layers • For ED > 1.1 J/cm², cellular surface morphology is observed <ul style="list-style-type: none"> ▪ 80-300 nm long pillars (~90%Ge) underneath the surface corresponding to cell walls ▪ In between the walls, the Ge content below is lower than the initial content <p>Proposed mechanism: A high-R l/s interface leads to faceting and finally to Ge segregation into pillars</p>

3. Investigation of laser annealing on patterned $\text{Si}_{1-x}\text{Ge}_x$ structures

In this section, results on the top-down patterning of $\text{Si}_{1-x}\text{Ge}_x$ substrates are presented with the goal of preparing dedicated nanopatterns for the study of laser annealing on relaxed and strained $\text{Si}_{1-x}\text{Ge}_x$ substrates. The first part demonstrates the successful lithography and etching techniques for vertical nanostructures as elaborated on thick layers of relaxed $\text{Si}_{0.8}\text{Ge}_{0.2}$ and $\text{Si}_{0.5}\text{Ge}_{0.5}$ which are relevant for the sample preparation as described in the second section as well as the nanostructure preparation for silicidation experiments following the procedures outlined in WP2. The second part focuses on the design and fabrication of nanopatterned SiGe surfaces for laser anneal studies to be realized on SiGe substrates with different strain and Ge concentrations. We present the current design and first lithography results for dense nano-line arrays.

3.1. Optimization of vertical patterning processes for SiGe substrates

The nanostructuring of SiGe substrates for different applications and experiments can be achieved through the creation of nanostructured e-beam resist masks and successive transfer etching of the design into the substrate or by directly creating SiO_2 structures through the electron beam lithography (EBL) of Hydrogen Silyloquinone (HSQ), a negative-tone resist mask. HSQ is a suitable candidate for both approaches as the negative resist allows to achieve high resolutions and highly vertical resist structures.

For the EBL a Raith-150 system is used at minimal spot size and an acceleration voltage of 30 kV, allowing for the fast exposure of dedicated star-shaped writing patterns to achieve round shapes. While achievable EBL pattern sizes and thus fabricated nanostructures are limited to 25-30 nm diameters, the reduced overall writing time makes this approach applicable for larger structures and even wafer scale processing.

The exposed resist layer is developed in 25% Tetramethylammonium hydroxide (TMAH) and rinsed in Methanol prior to drying. The obtained nano-patterns are then transferred onto the $\text{Si}_{1-x}\text{Ge}_x$ substrates by fluorine-based anisotropic reactive ion etching (RIE) in an Alcatel AMS4200 system within an inductively coupled plasma (ICP-RIE) chamber. The etching recipe is adjusted to each type of substrate in order to have perfectly vertical nanostructures with 200 nm height. Etched nanostructure samples are subsequently submerged in diluted hydrofluoric acid to remove the remaining HSQ mask, followed by a low-power oxygen plasma cleaning to remove any carbon residues that are introduced through the primary plasma etching process.

3.1.1. Characterization of bulk substrates

We used SiGe substrates provided by J.-M. Hartmann from CEA-LETI which were fabricated through epitaxy on slightly p-type Si(001) substrates of (i) SiGe linearly graded layers from a few %Ge up to the targeted Ge concentrations (20% or 50%), with 10% μm^{-1} ramps, followed by (ii) more than 1 μm thick $\text{Si}_{0.8}\text{Ge}_{0.2}$ or $\text{Si}_{0.5}\text{Ge}_{0.5}$ layers. Such depositions were conducted at 20 Torr with a $\text{SiH}_2\text{Cl}_2 + \text{GeH}_4$ chemistry in a 200 mm single wafer Reduced Pressure – Chemical Vapour Deposition cluster tool. The epitaxy temperature, 900°C for $\text{Si}_{0.8}\text{Ge}_{0.2}$ and 850°C for $\text{Si}_{0.5}\text{Ge}_{0.5}$, was high enough to promote the glide of the threading arms of misfit dislocations in the graded layers, resulting in almost strain-free constant composition SiGe layers on top with a reduced threading dislocation density, typically around 10^5 cm^{-2} . The surface cross-hatch typically present on such SiGe virtual substrate was suppressed thanks to

dedicated Chemical Mechanical Polishing process steps, with a removal of $\sim 0.5 \mu\text{m}$ out of the initially $1.2\text{-}1.3 \mu\text{m}$ thick $\text{Si}_{0.8}\text{Ge}_{0.2}$ or $\text{Si}_{0.5}\text{Ge}_{0.5}$ layers.

The composition and thickness of the SiGe surface layers of the as-fabricated substrates was verified by SIMS measurement, conducted by P. Michałowski at IMiF, as presented in **Fig. 3.1(a,b)**. The surface layers show a homogeneous concentration of 50.7% and 20.9% of Ge over a depth of 723 nm and 781 nm respectively, in close agreement with the desired growth parameters.

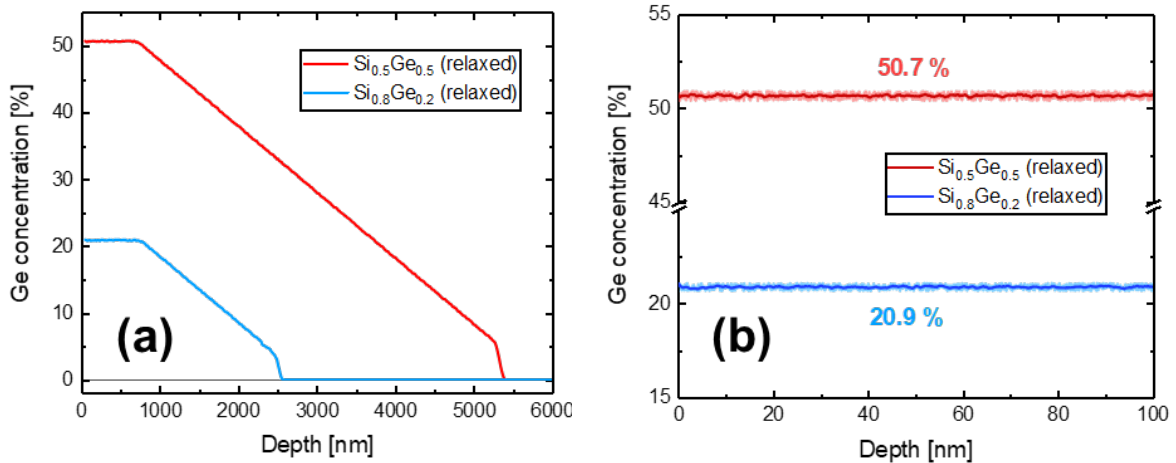


Figure 3.1: Plot of the measured SIMS profiles (IMiF) of the Ge concentration of bulk SiGe substrates provided by CEA which are used for lithography and etching tests. (a) Measurement of the relaxed and homogeneous surface layer and linearly graded transition layer, (b) magnified plot of the SIMS depth profile of the homogeneous surface layer.

3.1.2. Surface nanopatterning by e-beam lithography

The e-beam lithography of nanostructures such as nanosheets (NS) and nanowires (NW) is first tested using 90 nm thick HSQ with low acceleration voltage EBL (30 kV) and the same settings as used for the e-beam lithography on pure silicon as already presented in [6]. While rectangular nanosheets can be obtained with classical area exposure patterns, smaller and perfectly circular nanowire patterns require dedicated star shape patterns such as those proposed by Guerfi et al. [7]. HSQ patterns of $2.1 \mu\text{m}$ long beams for NS and different star designs with 12 or 36 branches for small or large NW designs are exposed with varying widths or diameters on the various types of $\text{Si}_{1-x}\text{Ge}_x$ substrates ($x = 0.2, 0.5$). The low Ge content in $\text{Si}_{0.8}\text{Ge}_{0.2}$ makes it similar enough to pure Si substrates so that well-known exposure parameters for Si do not require any adjustments to achieve the same resolution (**Fig. 3.2(a)**). For an increased Ge concentration however, the resolution is impacted by proximity effects enlarging NW structures by 10-20 nm (see plotted NW widths or diameters in **Fig. 3.2(c)**). Furthermore, the proximity effect and the accompanying charge accumulation can result in an agglomeration of resist for tightly spaced nanosheets. To prevent this, the exposure dose was reduced. A reduction by 20-30% depending on the nanosheet width was enough to suppress resist agglomeration. An additional reduction of the dose in order to further reduce the nanowire dimension was unfortunately not possible as the used settings were already close to the minimal dose. The obtained HSQ-nanomask for $\text{Si}_{0.5}\text{Ge}_{0.5}$ is presented in **Fig. 3.2(b)**. The smallest obtainable structure was 60 nm for the mixed array shown. It was shrunk down to 50 nm for widely spaced arrays with nanowires only. Smaller NW and NS structures were not feasible because of the interference of surface charges which accumulated during the writing

of the NS array, removing the smallest structures in a certain radius around the center of the NS array. For the given EBL setup, it was not possible to avoid this effect without re-designing the mask layout to have a proper spacing between NW and NS.

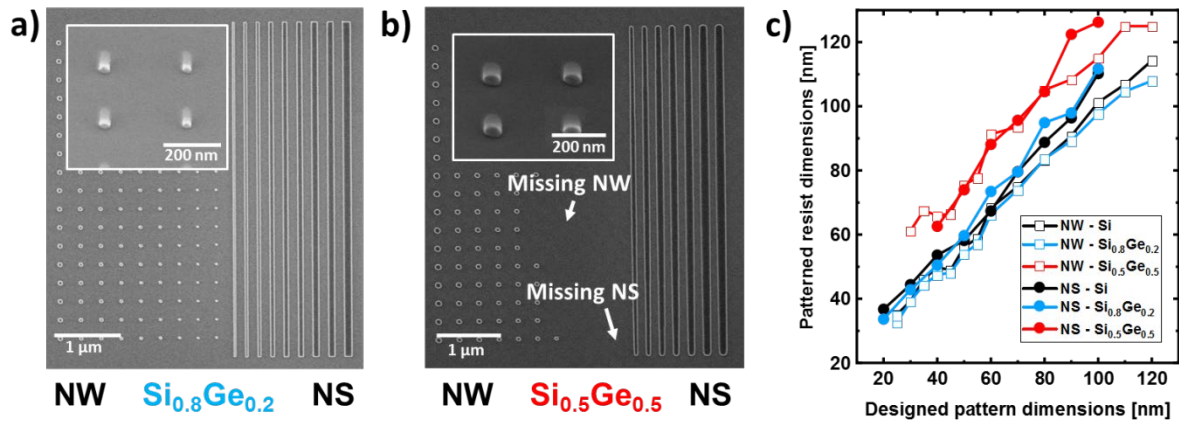


Figure 3.2: Scanning electron microscopy images of nanopatterned HSQ masks for a mixed array of nanowires and nanosheets of different sizes on relaxed $\text{Si}_{0.8}\text{Ge}_{0.2}$ (a) and $\text{Si}_{0.5}\text{Ge}_{0.5}$ (b). The HSQ structures have been measured on $\text{Si}_{1-x}\text{Ge}_x$ ($x = 0, 0.2, 0.5$) substrates. They are plotted over the designed pattern dimension in (c) for comparison. While the nanopatterning on $\text{Si}_{0.8}\text{Ge}_{0.2}$ behaves in the same way as on pure Si, the increased Ge content of $\text{Si}_{0.5}\text{Ge}_{0.5}$ causes all structures to be enlarged due to proximity effects. This is most obvious for dense nanosheet arrays and may result in agglomerated nanosheets and the removal of smallest NW and NS structures in the vicinity. The dose for $\text{Si}_{0.5}\text{Ge}_{0.5}$ patterns was reduced to minimize such effects.

3.1.3. Vertical etching of SiGe nanostructures

EBL fabricated nano-patterns are transferred onto the substrates by the same fluorine-based anisotropic reactive ion etching process previously optimized for 200 nm tall Si structures at CNRS-LAAS. Samples are pre-cleaned with a 15 s oxygen plasma, directly followed by the main etching step using a gas mixture of SF_6 , C_4F_8 and O_2 with constant pressure, power and overall flows. Right after etching, the structures have straight and smooth sidewalls. The HSQ mask is mostly resistant to the etching but suffers a rounding of the top edges and a shrinkage of the widened base diameter by a few nanometers. On average, the fluorine-based plasma etching reduces the initial HSQ thickness of 90-100 nm to roughly 50-60 nm with a high etching selectivity of 1:4 between HSQ (SiO_2) and Si and a good chemical stability.

Using the same conditions on SiGe yields similar results for low Ge concentrations but results in an undercut of the structures and increased surface roughness for higher Ge contents because of the increased chemical reactivity of Ge with the fluorine gas mixture. The SiGe etch rate is increased as compared to silicon which is expected as studies by Oehrlein et al. [8] demonstrated the etch rate increase for different SiGe substrates. While pure Ge is generally etched faster than Si, the etch rate of SiGe alloys does not only increase with the Ge concentration but also due to an increased halogen reaction rate. During the fluorine plasma etching, the structure's surfaces are enriched with Germanium which changes the electronic properties enabling a faster electron transfer between halogen and substrate [9]. Of course, the used fluorine compounds and their ratio also have a direct impact on the etching results: SF_6 has a much higher Si etch rate than C_xF_y . The difference is even higher when the Ge

content increases (e.g. as stated in [10]). The chemical reaction with the substrate will thus change. The less volatile SiO_xF_y passivation layer on the nanostructure sidewalls, which is largely responsible for the high anisotropy of the etching profile [11], may not be formed. To obtain highly anisotropic nanostructures, it is thus necessary to optimize the reaction foremost through the optimization of the composition of the used gas mixture.

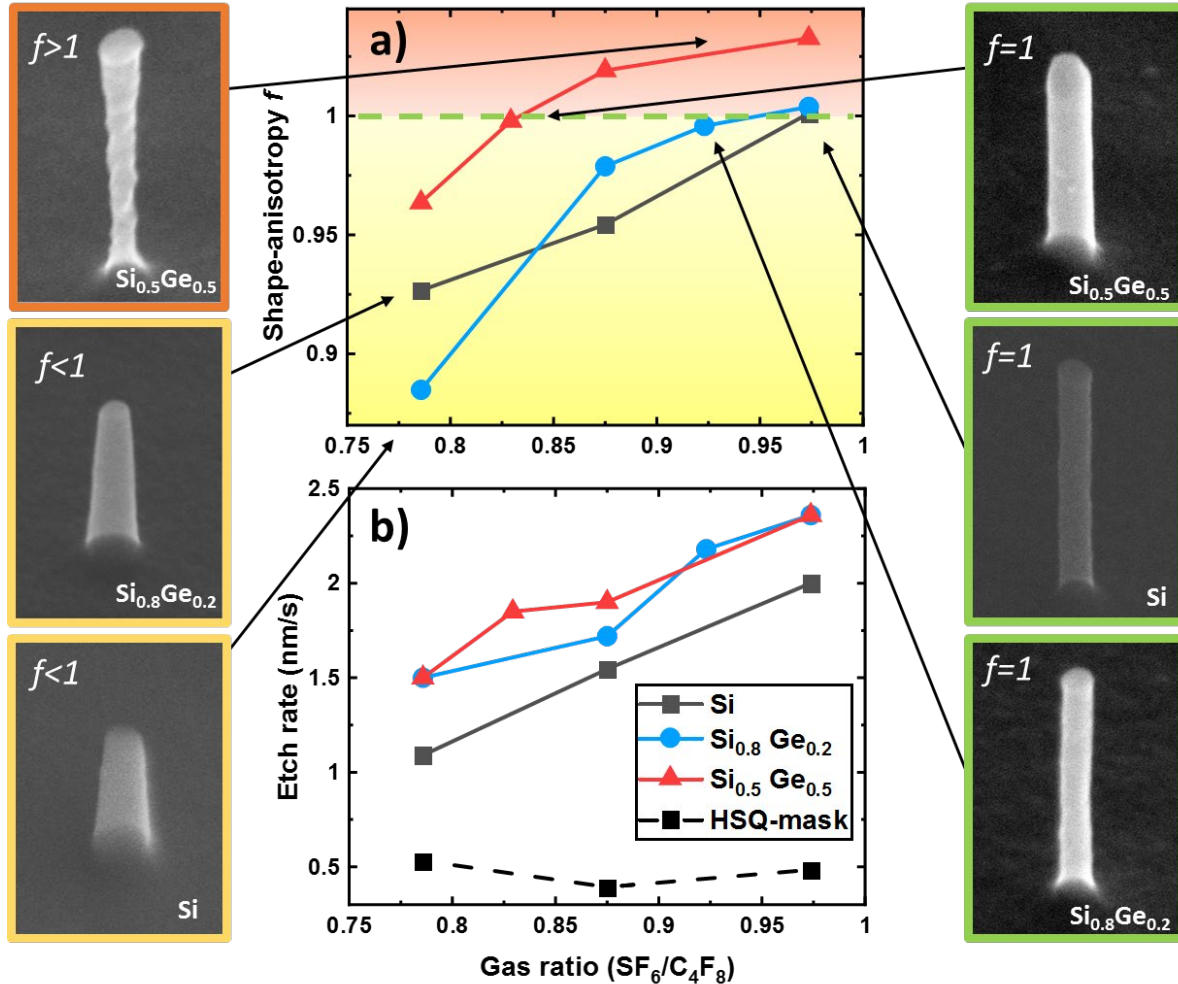


Figure 3.3: To achieve nanowires with perfectly straight sidewalls, the fluorine-based gas mixture of the RIE etching process has been optimized to achieve shape-anisotropy factors f of 1 ($f = 1 - (d_{\text{etch,rel}}/2 h_{\text{etch}})$, h_{etch} being the nanowire height and $d_{\text{etch,rel}}$ the relative change of the nanowire diameter from top to bottom). $\text{Si}_{1-x}\text{Ge}_x$ form-anisotropy factors together with $\text{Si}_{1-x}\text{Ge}_x$ and HSQ mask etch rates are plotted against the $(\text{SF}_6/\text{C}_4\text{F}_8)$ mass-flow ratio in (a) and (b), respectively.

Similar etching processes, with the same pressure, temperature and overall flows but with various $\text{SF}_6/\text{C}_4\text{F}_8$ ratios were tested on the $\text{Si}_{1-x}\text{Ge}_x$ substrates. The shape anisotropy factor f and etching speed for the substrates and the HSQ mask were measured thanks to SEM observations of processed nanowire arrays. They are given in Fig.3.3. In all cases, the NW shape becomes conical if the mixture is C_4F_8 rich. f increases logarithmically with the $\text{SF}_6/\text{C}_4\text{F}_8$ ratio for SiGe and nearly linearly for Si. The different behaviours indicate a different chemical interaction between the dominant fluorine species and the Ge in SiGe substrates. Meanwhile, the etch rate increases almost linearly for all substrates, with a nearly constant etch rate

difference between Si and SiGe. We can thus conclude that the variation of the shape-anisotropy factor is only caused by the changing chemical passivation reaction of either SF₆ or C₄F₈ with the etched germanium-rich sidewalls. We also note that the change of the gas mixture did not affect the HSQ mask which displayed a nearly constant etch rate for all tested gas mixtures. Based on the determined shape anisotropy curve, ideal gas mixtures for Si_{0.8}Ge_{0.2} and Si_{0.5}Ge_{0.5} were selected and perfectly vertical nanowires could be obtained, highlighting that the generic SF₆/C₄F₈ RIE etching process can be adjusted to be anisotropic for any SiGe substrates.

3.2. Fabrication of periodic nanostructures for laser annealing studies

3.2.1. Laser annealing of SiGe/SiO₂ interface

The effect of laser annealing in patterned arrays is of crucial importance for the assessment of the process features in device-like structures. The modulated and materials dependent absorption of the laser electromagnetic field and the multi-dimensional transport of the thermal energy usually lead to process results which are strongly different from those obtained in blanket samples. To study this effect, we proposed in the deliverables D4.2 and D4.4 the experimental realization of “mechanical demonstrators” made by patterned sequences of SiO₂ trenches which, in spite of the simplicity of the geometries with respect to the ones of real devices, should manifest the patterning effects and some common issues of the laser annealing process integration in devices manufacturing flow. The LA processes will be simulated in the same geometries realized according to the design of the experiments discussed in the following subsection and the simulation results will be reported in the upcoming deliverable D4.7 whilst the experimental characterizations of the irradiated sample will be the subject of further investigations in the project.

A preliminary result of the simulation study confirms some indications already reported in the deliverable D4.4. In particular, the process window for the occurrence of a melting laser annealing process depends on the geometry and it is shifted toward lower laser fluences. Moreover, the value on the melting threshold increases with decreasing ratio of the SiO₂ trench width and the structure pitch.

It is thus of interest to include multiple pattern geometries, combinations of SiO₂ line width and pitch, for the sample fabrication and successive experimental characterization.

3.2.2. Test fabrication of dense nanobeam arrays on relaxed SiGe

Dense SiO₂ nanobeam/line arrays of 30, 50, 70 and 80 nm width with varying pitches of 100-200 nm have been fabricated by e-beam lithography, as presented in Section 3.1.2, using 50 nm thin HSQ on relaxed Si_{0.8}Ge_{0.2} and Si_{0.5}Ge_{0.5}. As proximity and charging effects are enhanced for Ge-rich SiGe substrates, multiple dose test patterns (see **Fig. 3.4.(a)**) are created and observed in order to fine tune the lithography exposure setting for specific width/pitch combinations on Si_{0.8}Ge_{0.2} and Si_{0.5}Ge_{0.5} respectively.

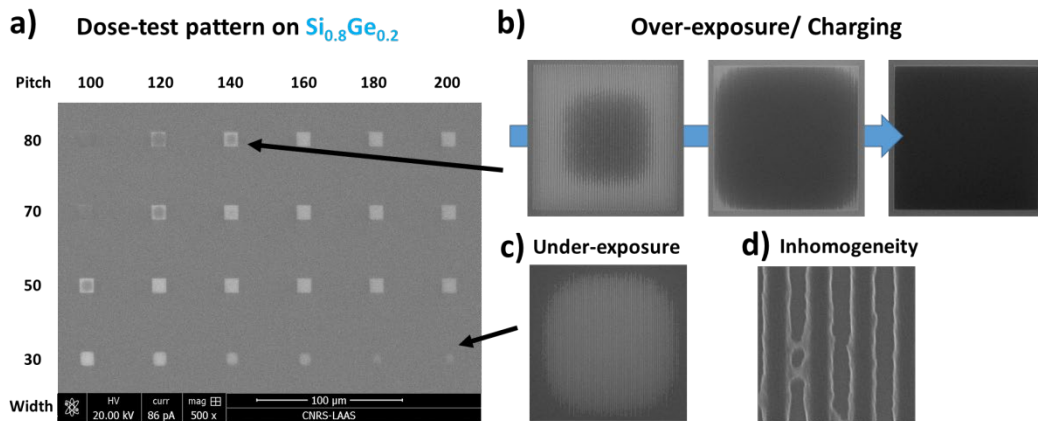


Figure 3.4: Scanning electron microscopy (SEM) images of nanopatterned HSQ line arrays on relaxed $\text{Si}_{0.8}\text{Ge}_{0.2}$ and $\text{Si}_{0.5}\text{Ge}_{0.5}$. Observed dose test patterns, for a given dose, exhibit over and under exposed arrays as highlighted in (b) and (c). The writing of dense lines causes a charge build-up over-time which causes strong proximity effects in the center of the array (b). The denser the lines are spaced, the stronger is the effect. Due to the same effect less dense arrays or low dosed patterns show line arrays where the center is well exposed while the edges are being removed. This dose discrepancy within arrays can also be observed as resist inhomogeneities and enlargement of the design features especially in the center (d).

Due to the high density of patterned lines of many arrays strong charging and proximity effects are observed which leads to an effective dose discrepancy from the center to the edge of the array. Highly dosed test patterns show arrays with over-dosing in the center while lowly dosed patterns appear well exposed in the center but reveal under-dosing near the edges/corners. Based on these observations a rough “dose-map” of feasible dose factors (DF) for desired width and pitch combinations has been created for both substrates. As presented in **Fig. 3.5** it is not possible to correctly expose densest arrays, possible minimal line spacings are 80 or 100 nm for $\text{Si}_{0.8}\text{Ge}_{0.2}/\text{Si}_{0.5}\text{Ge}_{0.5}$ so that smallest pitch dimension can only be realized for thin lines.

In addition, regardless of the selected dose parameters, structures are enlarged by roughly 10 nm at the foot of the created HSQ structures due to a sloped sidewall profile. While written pattern dimension have size variations of 40/60/80 nm, it is technically possible to further reduce the exposure dose in order to obtain 30 nm wide HSQ structures.

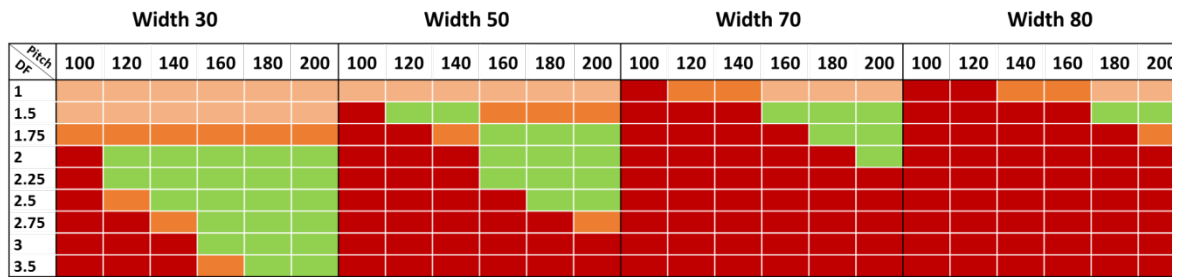
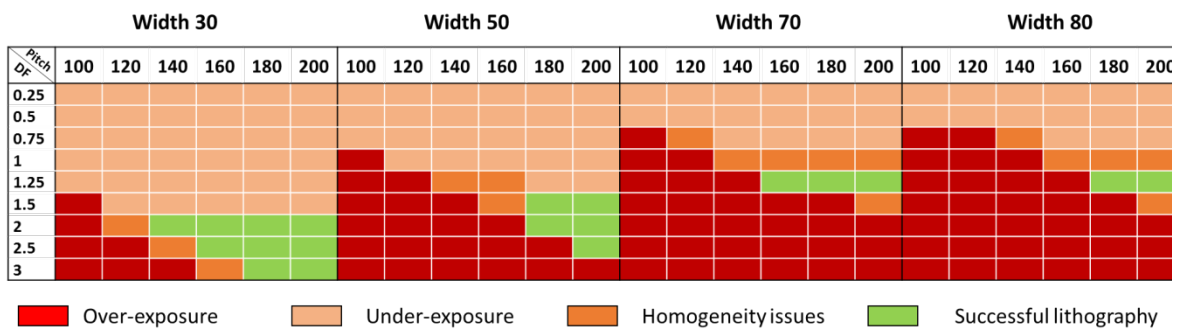
a) $\text{Si}_{0.8}\text{Ge}_{0.2}$ b) $\text{Si}_{0.5}\text{Ge}_{0.5}$ 

Figure 3.5: Quality map of the observed dose test patterns for different nanoline arrays with varying width and pitch dimensions (given in nm) for $\text{Si}_{0.8}\text{Ge}_{0.2}$ (a) and $\text{Si}_{0.5}\text{Ge}_{0.5}$ (b) and used dose factors (DF) during the e-beam lithography.

3.2.3. Sample fabrication for laser anneal studies

Based on the presented dose map, a full sample design is created where the different pattern geometries are attributed to individually optimized dose factors (DF). This is done for the already designed line widths of 30, 50, 70 and 80 nm with pitches of 100, 120, 140, 160, 180 and 200 nm in order to obtain the same widths at the SiGe/SiO₂ interface on both SiGe substrates. The obtained GDS (Graphic Design System) layout, as presented for the example of $\text{Si}_{0.5}\text{Ge}_{0.5}$, is shown in **Fig. 3.6(a,b)**.

First exposures with only the optimized dose factors achieved the expected line widths and desired quality of the pattern in the center and intermediate regions of the array. However, the outermost lines experience weakened proximity effects, less charge accumulation and hence a smaller effective dose. This causes a variation of the line width in the exposed structures towards the edge and increases the possibility of instabilities of the lines. To compensate this “edge-effect” the dose factor for the outermost lines has been increased by 0.05 and 0.1 respectively (see **Fig. 3.6(c)**) which sufficiently minimizes the size variation and prevents any rounding of the array by lines breaking off in the corners.

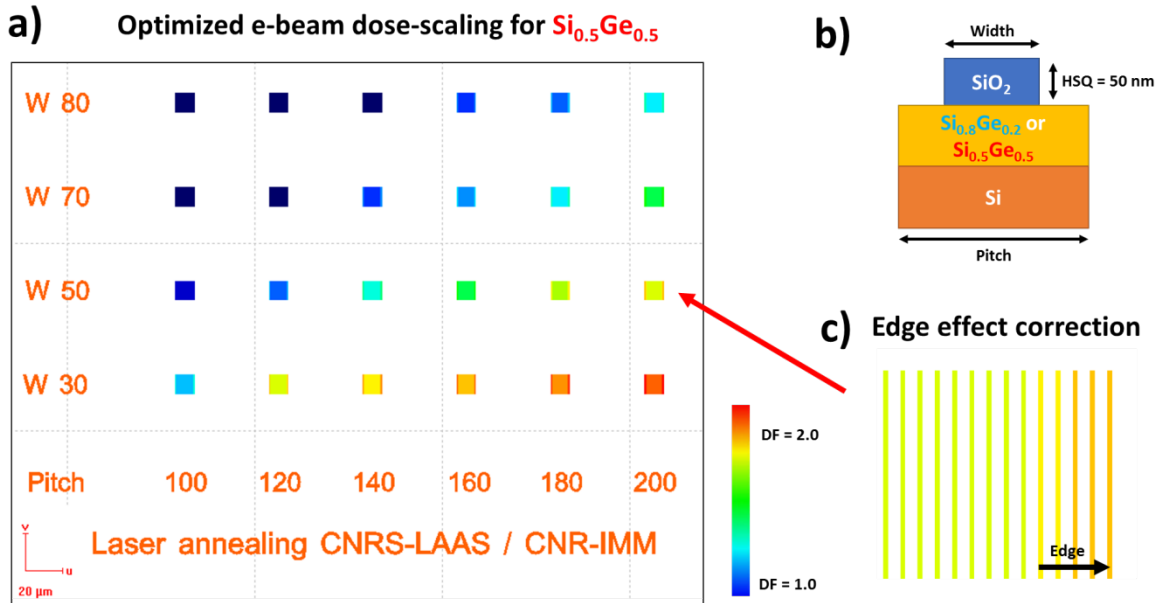


Figure 3.6: Final GDS (Graphic Design System) layout (a) for the sample fabrication of different geometries of nanoline arrays as illustrated in (b). The same width and pitch combination as previously used for the dose tests have been optimized by applying individual dose factors (DF, color range from blue to red) as indicated by the dose test map in Fig. 3.5 for $\text{Si}_{0.8}\text{Ge}_{0.2}$ (not shown) and $\text{Si}_{0.5}\text{Ge}_{0.5}$. In order to reduce the under-exposure of the lines near the edges of the arrays (edge effects), the dose factor of the outer most lines has been increased by 0.05 and 0.1 respectively, see (c).

HSQ line arrays using the final GDS patterns have been fabricated on both substrates and then characterized by scanning electron beam microscopy (SEM) as presented in Fig. 3.7. The average line width for all arrays has been measured within the intermediate region (see Fig. 3.7(b)) of the array and yields the desired widths of 30, 50 and 70 nm consistently across all pitches for $\text{Si}_{0.8}\text{Ge}_{0.2}$ and likewise 50 and 70 nm for $\text{Si}_{0.5}\text{Ge}_{0.5}$. While a near-30 nm line width on $\text{Si}_{0.5}\text{Ge}_{0.5}$ can be achieved for few geometries as presented in Fig. 3.7(a), an adjustment of the dose towards 30 nm leads to a significantly decreased stability and line yield, making those arrays unfeasible for experimental usage. The structures are thus maintained under non-ideal conditions with 33-40 nm line widths as shown.

Line arrays on $\text{Si}_{0.8}\text{Ge}_{0.2}$ appear edge-effect free with the exception of the densest arrays such as W30-P100, W50-P100, W70-P120 and W80-P140 where array corners are slightly rounded along with minor variations of the line width. For $\text{Si}_{0.5}\text{Ge}_{0.5}$, edge effects are either not observable or negligible as realizable arrays have wider pitches compared to $\text{Si}_{0.8}\text{Ge}_{0.2}$. While these minor imperfections could be improved upon, their impact on the laser annealing results is negligible and thus no further modification is required.

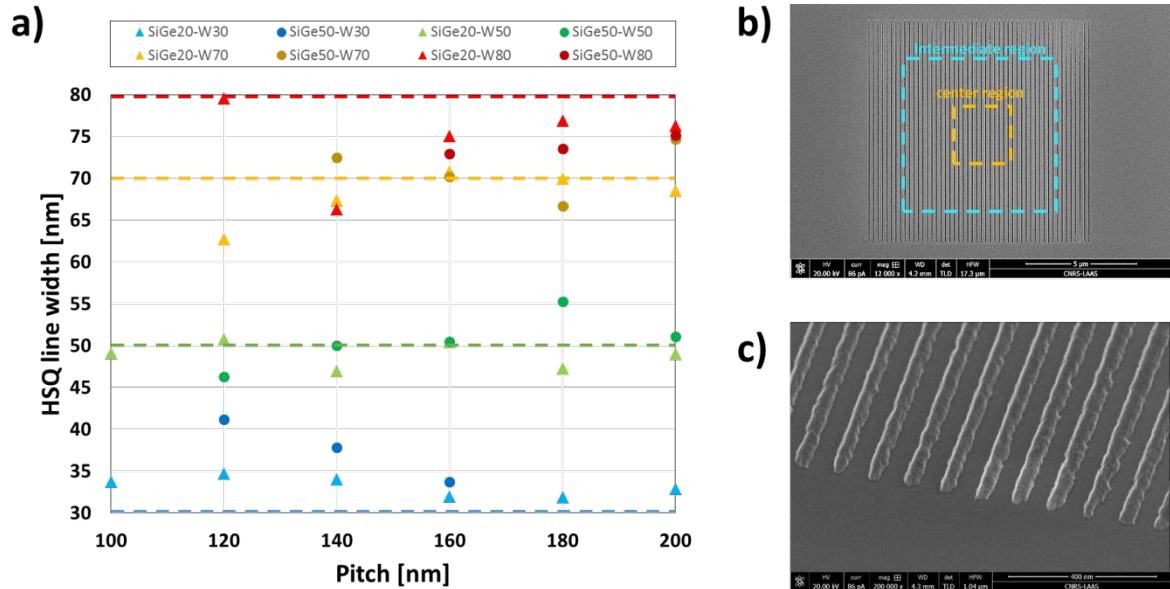


Figure 3.7: Observation and measurement of the HSQ-line width of the final nanoline arrays on $\text{Si}_{0.8}\text{Ge}_{0.2}$ (SiGe20) and $\text{Si}_{0.5}\text{Ge}_{0.5}$ (SiGe50) by SEM (a). Colored dashed lines are added as references for the targeted design widths. The line widths of all arrays on both substrates have been measured based on the intermediate regions as highlighted by dashed lines on a recorded SEM image in (b). The optimized dose factors lead to perfectly exposed lines with a tolerably small linewidth variation near the edge of the array and a negligible width fluctuation along the line of $\pm 2\text{-}4$ nm for both substrates ($\text{Si}_{0.8}\text{Ge}_{0.2}$ and $\text{Si}_{0.5}\text{Ge}_{0.5}$) as presented in (c).

3.3. Key information

Key information – Investigation of laser annealing on patterned Si _{1-x} Ge _x structures	
3.1.1	<p>Characteristics of relaxed Si_{0.8}Ge_{0.2} and Si_{0.5}Ge_{0.5} layers:</p> <ul style="list-style-type: none"> Fabricated by Reduced Pressure Chemical Vapor Deposition (RPCVD) and thanks to a thick SiGe buffer layer in between Si(100) substrates and final r-SiGe layers Ge content and ramps confirmed by SIMS measurements
3.1.2	<p>Surface nano-patterning of r-SiGe:</p> <ul style="list-style-type: none"> Process: Electron Beam Lithography combined with thin HSQ resist (previously developed for Si nanowire fabrication) Mask designing for nanosheets (NS) and nanowires (NW) fabrication Optimization of exposure dose for r-SiGe layers, taking into account proximity effect and charge accumulation <p>Best obtained resolution for NW and NS: ~30 nm (Si-rich); ~60 nm (Ge-rich)</p>
3.1.3	<p>Vertical etching of r-SiGe nanostructures:</p> <ul style="list-style-type: none"> Process: Reactive Ion Etching (RIE) with fluorine-based gas mixture: SF₆, C₄F₈ and O₂ (previously developed for Si nanowire fabrication) Optimization of SF₆/C₄F₈ gas ratio for each SiGe layer to achieve a shape-anisotropy factor of 1 <p>Perfectly vertical SiGe nanowires were obtained using an adjustable RIE process</p>
3.2.1	<p>Laser annealing of the SiGe/SiO₂ interface:</p> <ul style="list-style-type: none"> Laser annealing must be experimentally tested on patterned geometries to understand electromagnetic field absorption and thermal energy transport → design of SiO₂ trenches arrays Simulations on equivalent structures will be performed in parallel to experimental study
3.2.2	<p>Test fabrication of dense SiO₂ nanobeam arrays on r-SiGe:</p> <ul style="list-style-type: none"> Nanolines with varying pitches were fabricated based on EBL processing of HSQ resist Further EBL optimizations were made because of enhanced proximity and charge accumulation effects due to the high density of nanostructures <p>Obtained structures: ~40-80 nm with 100-200 nm pitches</p>
3.2.3	<p>Sample fabrication for laser annealing studies:</p> <ul style="list-style-type: none"> Fully optimized dose factors patterned geometries for NLA experiments have been fabricated with previously tested nanoline designs An “edge effect” on outermost lines has been observed and rigorously compensated Best resolutions obtained: <ul style="list-style-type: none"> For Si_{0.8}Ge_{0.2}: 30-70 nm width with 100-200 nm For Si_{0.5}Ge_{0.5}: 50-70 nm width with 120-200 nm (due to higher Ge content) <p>Samples are ready for NLA experiments</p>

4. Dopant activation in laser annealed strained SiGe layers

As discussed in detail in the previous report D4.3 as well as sections of this deliverable, SiGe alloy suffer from structural and alloy stoichiometry modifications when using laser annealing, particularly in melt conditions. These substantial alterations might affect the activation and the distribution of dopant as well as their electrical properties. This section aims to extend the first experimental investigations made on undoped SiGe layers to boron-doped SiGe layers (**T4.2**) in order to evaluate the impact of laser annealing on the activation of dopants. First, we describe the experimental details from the fabrication conditions and the sample characteristics to the different characterization methods used. Then, a part is dedicated to the identification of the laser regimes and their associated strain state inside the layers. Finally, the last part focuses on the study of boron activation in the same layers, as a function of the energy density and taking into account their structural condition.

4.1. Experimental details and characterization techniques

4.1.1. Fabrication process and laser annealing conditions

In situ boron-doped 30 nm-thick pseudomorphic $\text{Si}_{0.7}\text{Ge}_{0.3}$ layers were grown by RPCVD (Reduced Pressure Chemical Vapor Deposition) in a 300mm Epsilon 3200 tool from ASM at 550°C, 20 Torr on top of a lowly phosphorus-doped Si (100) layer of 100nm, itself on top of p-type Si(100) substrates. The growth of these layers was performed by tuning the flux ratio of B_2H_6 / SiH_2Cl_2 precursors concurrently with GeH_4 , SiH_4 and Si_2H_6 precursors. Before SiGe:B and Si:P layers deposition, a 5%HF wet cleaning followed by an in-situ H_2 bake at 1100°C were used in order to obtain epi-ready Si surfaces. Three different levels of boron concentration were incorporated inside the layers: $7.3 \times 10^{19} \text{ cm}^{-3}$ (**A**), $1.3 \times 10^{20} \text{ cm}^{-3}$ (**B**) and $2.3 \times 10^{20} \text{ cm}^{-3}$ (**C**), corresponding to 100%, 80% and 60% boron activation (**Table 4.1**), respectively (reported in **D3.3**). These levels of activation have been chosen intentionally to emphasize the different effects of nanosecond laser annealing (NLA)

Name	SiGe layer thickness	Ge content	B doping
A	30 nm	30 %	$7.3 \times 10^{19} \text{ cm}^{-3}$
B			$1.3 \times 10^{20} \text{ cm}^{-3}$
C			$2.3 \times 10^{20} \text{ cm}^{-3}$

Table 4.1: Characteristics of boron-doped SiGe30% used in this section.

UV-NLA was performed with a SCREEN-LT3100 system, equipped with a XeCl excimer laser (308 nm wavelength, ~145 ns FWHM pulse duration, 3% non-uniformity), while maintaining a constant flow of pure N_2 in the irradiated region. Areas of $15 \times 15 \text{ mm}^2$ were exposed to single laser pulses at various energy density values, ranging from 1.40 to 2.40 J/cm^2 , crossing all main laser regimes, from sub-melt to complete melt of the SiGe layers and above.

4.1.2. Characterization and analysis methods

Several characterization methods were used for this task. Hall Effect (HE) measurements were performed using a HL5500PC prober bench from Nanometrics. In-situ Time-Resolved Reflectivity (TRR) at 635 nm was used to detect the melt threshold and estimate melt duration. Strain and crystallinity were studied by High Resolution X-Ray

Diffraction (HR-XRD). Reciprocal space maps (RSM) around the (224) reflection were acquired with an X'Pert Pro PANalytical tool. Secondary ion mass spectrometry (SIMS) measurements have been performed with the CAMECA IMS SC Ultra instrument. Cs⁺ ions with ultra-low impact energy (100eV) have been used as a primary beam with an incident angle of 75°. Additional information on crystalline quality and germanium depth profiles was inferred from Transmission Electron Microscopy (TEM) observations performed with a JEOL JEM-ARM200F, coupled to Energy Dispersive X-ray (EDX) micro-analysis.

4.1.3. Activation analysis method

The activation level has been calculated using the unidimensional Boltzmann equation under consideration of the Hall effect (**Eq. 4.1, 4.2 and 4.3**). This algorithm compares Hall effect measurements (sheet resistance R_S , Hall mobility μ_H and Hall dose/sheet concentration N_H) to parameters calculated from SIMS profiles [12]. We define two fitting parameters: a uniform active doping level n_{elec} used as an adjustable filter to the boron SIMS profile [8,9] and α , a transport degradation factor accounting for the possible impact of the inactive dopant fraction or of the surface morphology on the carrier transport mechanism. Due to the high quality of the CVD fabrication process, the assumption of a uniform active doping level n_{elec} is most likely accurate, whether it is fully activated or not. Concerning the α factor, it is equal to unity when there is no transport degradation and smaller than unity otherwise. The different scattering phenomena are also considered through the Hall scattering factor r_H , which depends on the Ge fraction. **Fig. 4.1** shows the variations of r_H for strained SiGe alloys [13-20].

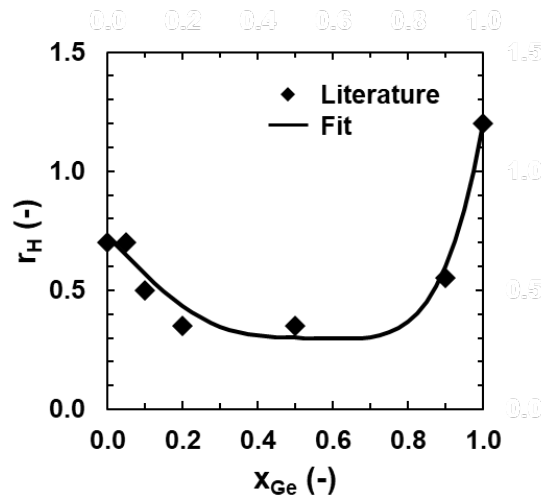


Figure 4.1: Hall scattering factor as function of the Germanium fraction considering a compressive strain in the SiGe alloy.

The algorithm works through two steps. First, from the filtered SIMS profile, the active doping level n_{elec} is tuned until both calculated and measured Hall doses match.

$$N_{H_{calc}} = \frac{\left[\int_0^d n_{elec}(z) \langle \mu(z) \rangle dz \right]^2}{r_H \int_0^d n_{elec}(z) \langle \mu^2(z) \rangle dz} \quad (4.1)$$

Once the maximum active doping level, n_{elec} , is determined, the calculated values are adjusted to the measured sheet resistance and the Hall mobility via the transport degradation factor α .

$$R_{S_{calc}} = \frac{1}{\alpha q \int_0^d n_{elec}(z) \langle \mu(z) \rangle dz} \quad (4.2)$$

$$\mu_{H_{calc}} = \frac{\alpha r_H \int_0^d n_{elec}(z) \langle \mu^2(z) \rangle dz}{\int_0^d n_{elec}(z) \langle \mu(z) \rangle dz} \quad (4.3)$$

From the final electrical boron profile, the active boron dose can be calculated and compared to the chemical boron dose to estimate the activation rate Ω .

4.2. Structural investigation boron-doped $\text{Si}_{1-x}\text{Ge}_x$ layers upon NLA

4.2.1. Laser regimes identification

From the previous analysis and reports, four distinct melt regimes were observed when annealing $\text{Si}_{1-x}\text{Ge}_x$ thin layers by laser: the sub-melt, surface melt, partial melt and full melt regimes (order of apparition when increasing the laser energy density) [10]. In the case of boron-doped layers, the thresholds between each regime are not impacted by the amount of incorporated boron. The corresponding laser regimes, as function of the energy density, are presented in **Fig. 4.2(a)** for all three layers.

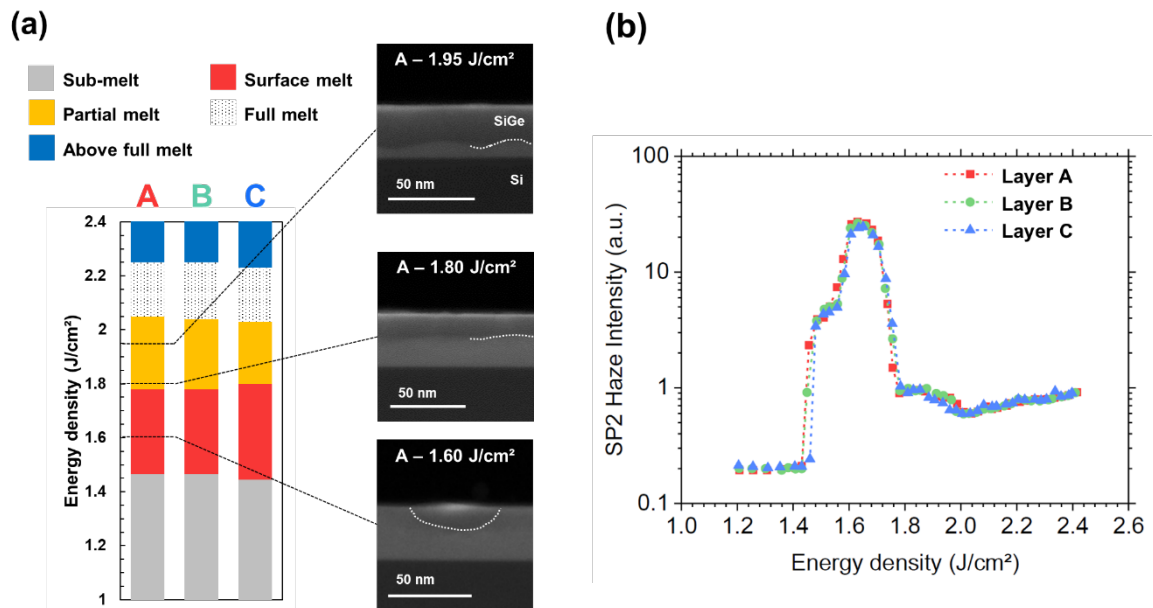


Figure 4.2: (a) Laser regimes as function of the energy density for our three boron-doped SiGe layers (A, B and C). Next to the histogram TEM images highlighting the progress of the liquid/solid interface are shown. The contrast observed at the interface results from the germanium redistribution in the recrystallized region, due to a partition coefficient smaller than unity. (b) Haze measurements as function of the energy density on the three studied layers.

Regime transitions have been identified by gathering data from several techniques: TRR, TEM and haze. TRR allowed to detect the early stages of the melt thanks to the significant change

in reflectivity involved by the phase change from solid to liquid (not shown). Thanks to the Ge redistribution occurring when reaching melt condition, TEM images enable, not only to discriminate surface and partial melt but also to evaluate the melt depth as function of the energy density. In addition, haze measurements give the possibility to precisely identify sub-melt to surface melt and surface melt to partial melt transitions, observable through the abrupt increase around 1.4 J/cm^2 and decrease around 1.8 J/cm^2 , respectively.

4.2.2. Strain relaxation phenomenon and energy density

For each laser regime, HR-XRD reciprocal space mappings (RSM) around the (224) diffraction axis have been used to evaluate the strain state of the layer at different energy densities, by comparing the position of the $\text{Si}_{0.7}\text{Ge}_{0.3}:\text{B}$ layer spot to the Si spot. **Fig. 4.3(a)** shows an overview of the strain state evolution of the three boron-doped $\text{Si}_{0.7}\text{Ge}_{0.3}$ layers depending on the energy density. In addition, the degree of relaxation calculated at different energy densities as discussed in **D4.3** supported by RSM mappings and TEM weak beam images [10] is presented in **Fig. 4.3(b)**. Supplementary measurements might be required to precisely assess the regimes of the threshold values (undetermined regions). However, the coupling of optical measurements with structural analysis (TEM) allows a good understanding of the strain state evolution. The calculations from RSM indicate a compressive strain up to the beginning of the melt, a partial relaxation between the beginning of the melt and close to the full melt (depending on the initial doping) and then, a recovery of the compressive strain when the underlying Si is involved in the melt region.

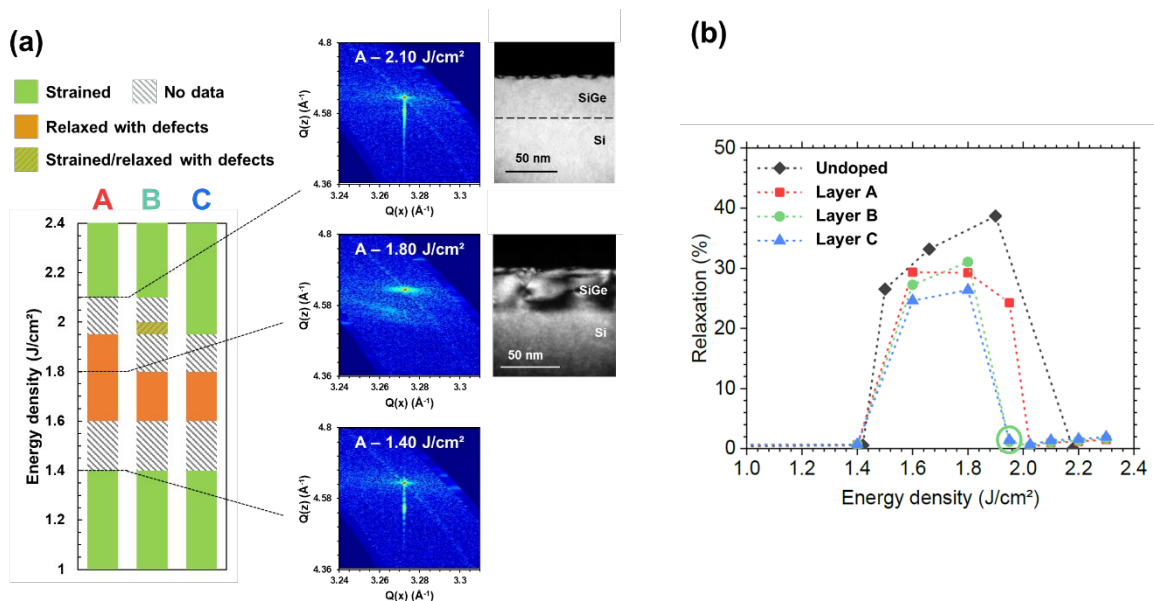


Figure 4.3: (a) Strain state as function of the energy density for our three boron-doped SiGe layers (A, B and C). HR-XRD RSM and weak beam images for the lowly-doped SiGe layer are shown next to the histogram to support the data and give a visual representation of the strain evolution. (b) Relaxation as function of the energy density for the three studied layers. An indeterminate value is indicated by a circle for layer B as RSM indicates a strained layer with residual relaxation and TEM images show a lot of defects, characteristic of partial relaxation in lower energy density conditions.

For the sub-melt regime, no significant change is observed by TEM (flat surface, no defects) and in the boron/germanium SIMS profiles (flat profiles, **Fig. 4.4**). When reaching the

partial melt regime, crossing defects (mainly stacking faults and misfit dislocations) appear in the melted and unmelted regions (see weak beam TEM images in **Fig. 4.3 (a)**) and, according to our calculations based on RSM, involve a partial relaxation in the whole layer (see **Fig. 4.3 (b)**). During the recrystallization of the layer, the germanium is not redistributed uniformly, as shown in **Fig. 4.4**. At higher energy densities (i.e. at the full melt and above), the layers recover a fully compressive strain state with no defects. The associated RSM are comparable to the sub-melt regime ones except that we do not observe distinct fringes due to Ge redistribution in the whole layer, with a Ge content between 10% and 80% (see **Fig 4.4 and 4.5**).

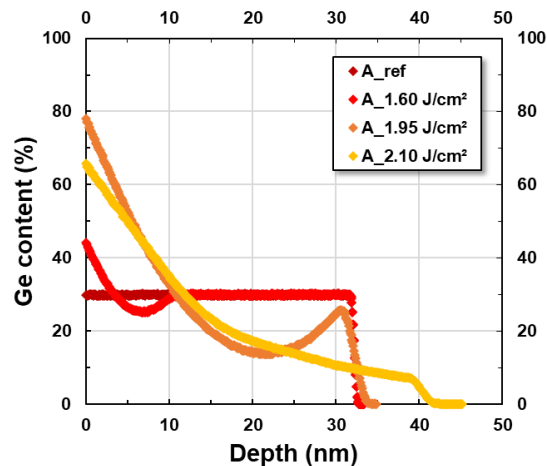


Figure 4.4: Germanium depth profiles of the mediumly boron-doped $\text{Si}_{0.7}\text{Ge}_{0.3}:\text{B}$ layer (A) annealed by laser at different energy densities along with the reference profile.

4.2.3. Strain recovery threshold difference due to doping

While all laser regimes are approximately invariant with the doping level, the strain regime thresholds differ when it comes to compressive strain state recovering at high energy densities. The RSM measurements made at the specific energy density of 1.95 J/cm^2 allows to highlight appropriately this difference (see **Fig 4.5**). For the lowly and highly doped SiGe layers, we are in a clear case of partial relaxation (with defects) and compressive strain (with no defects), respectively (**Fig 4.5(a,c)**). However, for the mediumly doped SiGe layer, the RSM shows spots aligned with Si spot but each of them with a diffused halo, leading to an intermediate state between layer A and C (**Fig. 4.6 (b)**). These results demonstrate that the incorporated dose of boron has an influence on the energy density threshold for strain recovery. It is favoured for the highly doped layers as substitutional dopants (supposedly at reaching the maximal active dose when close to the full melt) reduces the average lattice parameter of the SiGe:B layer. In this case and contrary to layer A and B, the stored elastic energy is lowered and the layer can recrystallize being compressively strained.

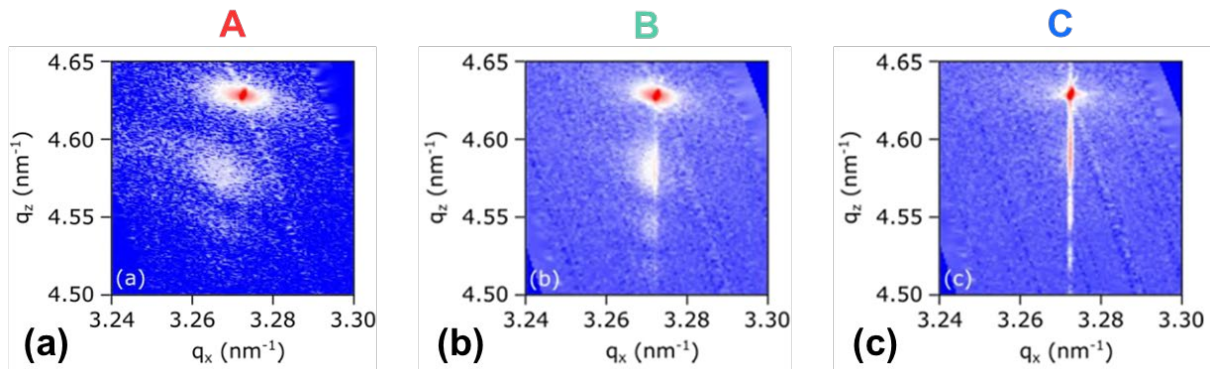


Figure 4.5: Reciprocal Space Maps along the (224) direction for boron-doped $\text{Si}_{0.7}\text{Ge}_{0.3}$ layers on Si and annealed at 1.95 J/cm^2 , for low (a), medium (b) and high (c) incorporated boron levels.

4.3. Electrical properties of $\text{Si}_{0.7}\text{Ge}_{0.3}:\text{B}$ layers annealed by NLA (CEA)

In deliverable **D3.3** was detailed the conditions of fabrication of the three wafers corresponding to our three different boron-doped strained SiGe layers. Also, a large number of characterizations of the thickness and the germanium content were made by optical measurements, particularly with X-Ray Reflectometry (XRR), X-Ray Diffractometry (XRD) and Spectroscopic Ellipsometry (ES), to confirm the good uniformity of the wafers. In addition, a preliminary study of the initial activation was made using Hall effect measurements (LAAS-CNRS) coupled with SIMS profiles (IMIF) and using the activation analysis method presented in 4.1.3. We took advantage of the electrical measurements presented and analysed in the following section to refine the algorithm used for the activation evaluation and for boron and germanium SIMS profiles calibration.

4.3.1. Activation in $\text{Si}_{0.7}\text{Ge}_{0.3}$ as-grown layers

The activation level inside the as-grown layers was evaluated using the activation algorithm presented in Section 4.1.3, Hall effect measurements and SIMS profiles shown in **Fig. 4.6(a)**. For now, the presence of boron peaks close to the surface remains unexplained, possibly being a measurement artefact or due to boron segregation at the native oxide/SiGe interface. In order to take into account the mentioned possibilities, the activation was calculated for both raw and filtered SIMS profiles (concentration filter was fixed at the plateau's value). For raw SIMS profiles, we find activation rates of 86% (A), 65% (B) and 46% (C) (**Fig. 4.6(b)**) and for filtered SIMS profiles, 91% (A), 61% (B) and 49% (C). Filtering the boron peak does not significantly increase these values ($\sim 3\text{-}5\%$). The associated active concentration levels are: $7.2 \times 10^{19} \text{ cm}^{-3}$, $1.1 \times 10^{20} \text{ cm}^{-3}$ and $1.45 \times 10^{20} \text{ cm}^{-3}$ compared to the chemical plateau measured by SIMS of $7.8 \times 10^{19} \text{ cm}^{-3}$, $1.6 \times 10^{20} \text{ cm}^{-3}$ and $2.9 \times 10^{20} \text{ cm}^{-3}$.

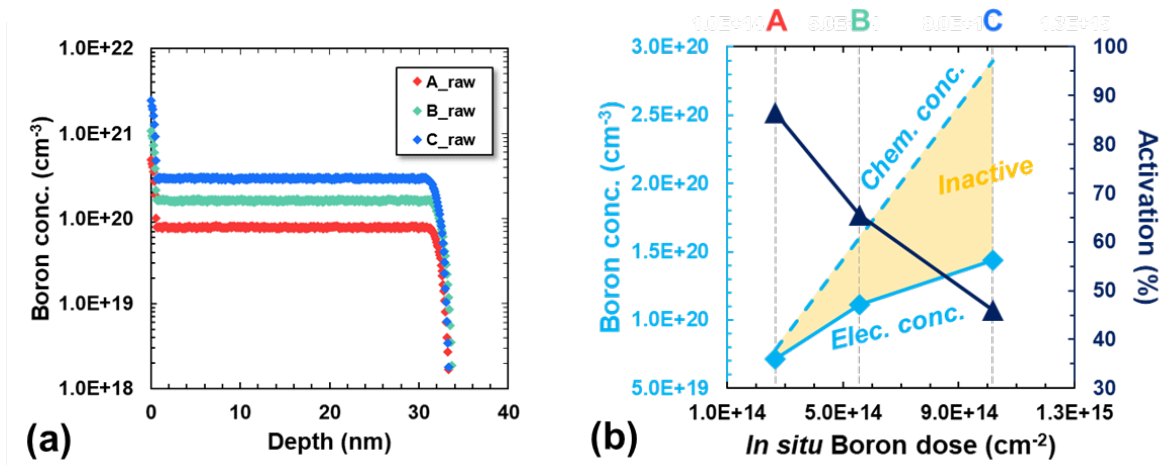


Figure 4.6: (a) Raw boron SIMS profiles of the as-grown layers A, B and C. (b) Electrical and chemical (from SIMS profiles) boron concentrations along with their associated activation rates for in situ SiGe:B layers in as-grown conditions.

The transport degradation factor α , plotted in **Fig. 4.7 (a)**, was also extracted. The calculated values are between 0.97 and 1, with an estimated deviation of around 5%, meaning that there is no transport degradation inside our layers, whether being fully or partially activated. To confirm this result, Hall mobility measurements as function of the temperature (between 20 K and 300 K) were performed on the lowly (A) and highly (C) doped SiGe:B layers and are shown in **Fig. 4.7 (b)**. The obtained curves demonstrate two clear behaviours: a surface scattering contribution over the whole range of temperature ($T^{-0.015}$), which is overshadowed by phonon scattering at high temperatures ($T^{-0.38}$ between 150 K to 300 K). Also, the similarity between the A and C curves corroborates the equivalent electrical transport in these layers, and so, the alpha coefficient results.

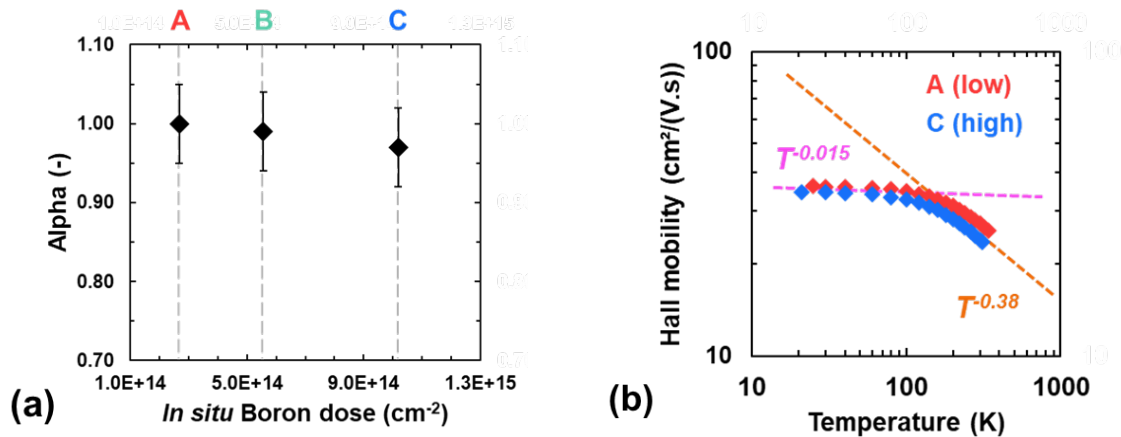


Figure 4.7: (a) Transport degradation factor α as function of the in situ boron dose in the studied SiGe:B layers. (b) Evolution of the Hall mobility as function of the temperature for the lowly (A) and highly-doped (C) as-grown SiGe:B layers. Slope coefficients are indicated next to their respective logarithm tendencies, corresponding to phonon scattering (orange) and surface scattering (pink).

4.3.2. Sheet resistance variations with energy density

Sheet resistance measurements by 4 point-probe (4PP) were made for all laser conditions. The evolution of the sheet resistance as function of the energy density for the three layers are shown in **Fig. 4.8 (a)**. As they are based on more data points, these curves can be used to complete the identification of the laser regimes and the strain state evolution with the energy density. To support the understanding of these curves, we also calculated their first derivative using a Savitzky-Golay algorithm (**Fig. 4.8 (b-d)**).

In terms of electrical transport, it is important to mention that, considering an equal number of active dopants, the carriers inside a strained SiGe layer will have a higher mobility than inside a relaxed SiGe with defects (see part 4.2.2) [22-24]. As a consequence, with regards to the sheet resistance, the former layer will have a lower sheet resistance than the latter one. Knowing this, we can see that the lowly-doped SiGe layer is more strongly impacted by the strain state of the layer as the sheet resistance variations are the clearest. This statement seems relevant as this layer is almost completely activated, and so, its transport properties should vary only according to its strain state, contrary to the mediumly and highly doped SiGe layers.

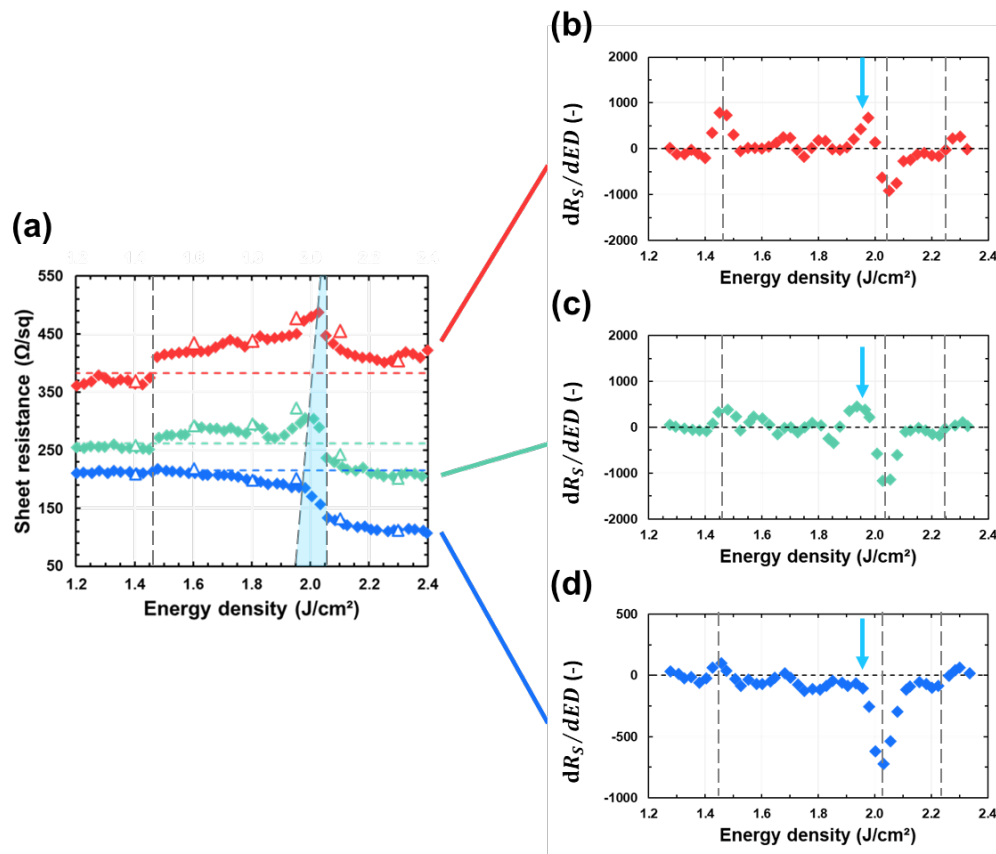


Figure 4.8: (a) Evolution of the sheet resistance R_S with the energy density for a lowly, a mediumly and a highly boron-doped strained $\text{Si}_{0.7}\text{Ge}_{0.3}$ layer annealed by NLA. Dark grey dashed lines represent different transitions (from left to right): sub-melt to surface melt, partially relaxed to strained, and partial melt to full melt. (b-d) 1st derivative of the sheet resistance curve using a Savitzky-Golay algorithm for each layer. Sub-melt to surface melt, partial melt to full melt and full melt to above full melt transitions are indicated with black dashed lines. Behaviour of dR_S/dED around 1.95 J/cm^2 related to **Fig. 4.5(a-c)** are indicated with a light blue arrow.

By using the sheet resistance profile along with its first derivative and comparing them with the existing data on laser regimes and strain states, we can distinguish at least four main transitions for the three layers:

First, around 1.45 J/cm^2 , there is a sharp increase of R_S in layers A and B, which is not clear for layer C (**Fig. 4.8 (a)**). This discontinuity is identifiable in the derivative curves by a positive peak around the 1.45 J/cm^2 for all three layers (**Fig. 4.8 (b-d)**). Concerning the strain state, this region is right in between a strained and a relaxed regime (**Fig. 4.3(a)**) and fits perfectly with the beginning of the surface melt identified by haze measurements (**Fig. 4.2(b)**). Thus, the sheet resistance first derivative variations confirm the sub-melt/surface melt threshold and the concomitant apparition of defects inside the layer, leading to partial relaxation.

Then, when irradiating the layers at an energy density around 1.8 J/cm^2 , surface and structural characterizations emphasized the beginning of the partial melt. Concerning the sheet resistance, only small variations are observable in layer A and B in this range of energy density. In contrast to the surface melt, in which the melted region is small and so the dopant activation going forward into the partial melt regime involves two competing phenomena: the activation of dopants and the transport degradation due to relaxation and defects. For the layer A, as the large majority of dopants are initially activated, the impact of the partial relaxation dominates and leads to an increase of R_S with the energy density. For layer B, the sheet resistance values tend to slightly decrease, highlighting an equilibrium between the cited phenomena. In the case of layer C, R_S clearly decreases, showing a clear compensation of transport degradation thanks to the activation of a large number of dopants. Nevertheless, compared to already reported cases [25], the impact of the partial relaxation remains non-negligible.

Between 1.95 and 2.05 J/cm^2 , two noticeable phenomena occur: the strain recovery and the full melt (see **Tab. 4.2**). At 1.95 J/cm^2 , like already mentioned in Section 4.2.3 (see **Fig. 4.5**), layers A and B are still impacted by relaxation and/or defects, which results in a deteriorated sheet resistance. Although the increase in R_S might be due to the liquid/solid interface roughness (**Section 1**), it must be considered as a second order phenomenon compared to defects and partial relaxation. For layer C, the strain recovery allows to maintain the improvement of R_S when increasing the melt depth. Then, reaching energy densities between 1.97 and 2.03 J/cm^2 (depending on the doping level), the sheet resistance decreases drastically for the three layers (see **Tab 4.2** and **Fig. 4.8(a)**). On the contrary to strain recovery, the full melt threshold is not impacted by the amount of boron incorporated in the layers (2.05 J/cm^2 for all layers). Thus, these results strongly suggest that the sheet resistance improvement does not coincide with the full melt regime but with the respective strain recovery of each layer.

Layer	At 1.95 J/cm^2		Sheet resistance decrease (J/cm^2)		
	Strain state	Laser regime	Beginning (Strain recovery)	End (Full melt)	Width
A	Partial melt	Relaxed	2.03	2.05	0.02
B		Strained or relaxed with defects	2.00	2.05	0.05
C		Strained	1.97	2.05	0.08

Table 4.2: Summary of strain state and laser regimes found at 1.95 J/cm^2 along with the respective energy density values of the notable R_S improvement around 2.0 J/cm^2 .

Between 2.05 J/cm² and 2.25 J/cm², the sheet resistance keeps improving ($dR_S/dED < 0$), not only because the strain state is restored but also because the melt duration keeps increasing, and so the maximum temperature, without melting the Si substrate (up to 15%). This leads to an improvement of the layer quality.

At 2.25 J/cm², the first derivative of the sheet resistance crosses the 0 value and becomes positive, which happens consequently to the melt of the Si underneath the SiGe layers. In this regime, the boron and the germanium are diluted and redistributed within a deeper melted layer. At the first stages of the Si melting, this leads to a stabilization of the sheet resistance $R_S = 1/q \int n(z)\langle\mu(z)\rangle dz$ as the electrical concentration n decreases and the mobility μ and thickness z increases almost equivalently.

4.3.3. Activation calculation

The activation rates inside all the annealed layers were first calculated by not considering the strain state variations and using the Hall scattering factor curve of a strained SiGe layer (black curve, **Fig. 4.9(a)**). The results are shown in **Fig. 4.9(b,c,d)** (black diamond dots). Transitioning from sub-melt to surface melt (indicated with a light blue dotted line around 1.45 J/cm²) involves a decrease of the activation rate, which is more pronounced when reducing the number of dopants: 13%, 10% and 2%, for layers A, B and C, respectively. From 1.6 J/cm² to 2.1 J/cm², the activation rate increases up to 100%.

However, we have demonstrated in the previous sections that cross-layer defects appear at the beginning of the melt (~1.45J/cm²), leading to a partial relaxation inside the layers. The compressive strain is recovered close to the full melt depending on their initial incorporated dose of dopants (**Tab. 4.2**). In the energy density range corresponding to the apparition of defects, the electrical properties are significantly impacted (see 4.2.3) so that the partial relaxation and the presence of crystal defects has to be taken into account through the Hall scattering factor coefficient. We know from literature that the mobility of holes inside a biaxial-strained SiGe layer is enhanced, compared to a relaxed SiGe layer [22-24]. This is mainly due to the valence band splitting between light and heavy holes that involves a full occupation of the light-hole bands and so, a change of effective mass. The presence of stacking faults and misfit dislocations emphasizes the electrical properties difference between strained and relaxed SiGe by introducing scattering centres. The Hall mobility and the drift mobility are linked through the Hall scattering factor by $\mu_H = r_H \times \mu$. According to theory, $\mu(\text{SiGe}_{\text{strained}}) > \mu(\text{SiGe}_{\text{relaxed}})$, which, for a given Hall mobility measurement, leads to: $r_H(\text{SiGe}_{\text{strained}}) < r_H(\text{SiGe}_{\text{relaxed}})$. Aside from values for pure Si and Ge, r_H was modified by increasing values up to 30% (orange curve, **Fig. 4.9(a)**) to obtain the best possible fits for all layers (orange diamond dots, **Fig. 4.9(b,c,d)**). This empirical modification includes both partial relaxation phenomenon and the presence of defects, which cannot be easily discriminated.

For layer A, the final results combining both Hall scattering factor curves suggest a slight improvement or a stable value around 100% of the activation when increasing the energy density, compared to the reference layer. For layers B and C, the activation becomes better as the melt region goes deeper and deeper. This effect is enhanced for layer C right after reaching the surface melt as an important part of the dopants are inactive in the as-grown layer. By taking into account the crystal state of the layer, these results suggest that the possible deactivation phenomenon observed initially could not be substantial, which is consistent with the well-known advantageous effects of laser annealing regarding the activation of dopants [26].

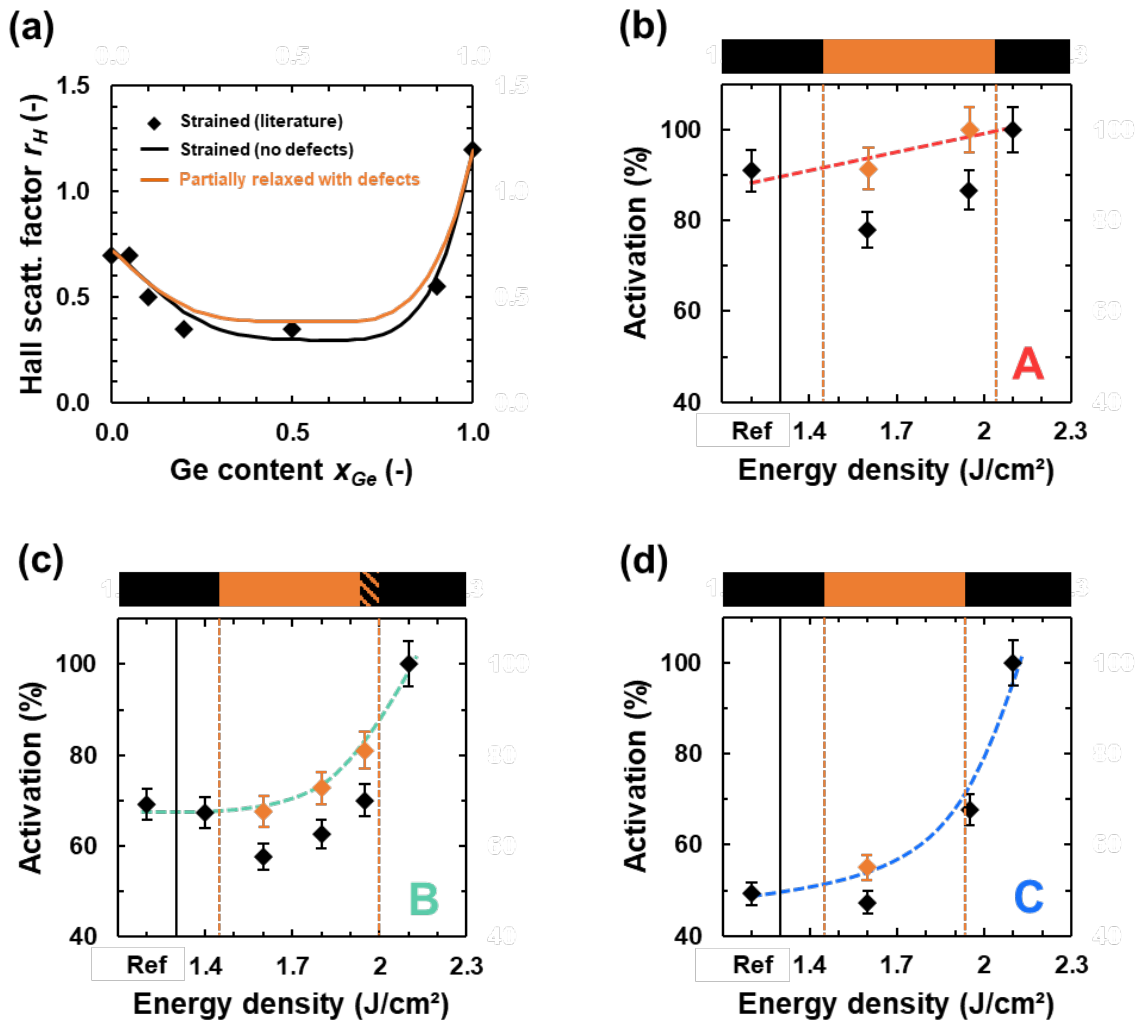


Figure 4.9: (a) Hall scattering factor as function of the germanium content for a strained SiGe layer and a relaxed (or strained) SiGe layer with defects (determined empirically). Evolution of the activation as function of the energy density for the layers A (b), B (c) and C (d), along with the activation in the as-grown layers. The strain state of the layers depending on the energy density are indicated above the graphs. Also, in order to highlight the impact of the strain state (and the crystal quality) on the activation, calculations in the partially relaxed range of energy densities (identified in Fig. 4.3(a)) have been made considering (orange diamonds dots) or not (black diamonds dots) the partial relaxation.

For the sake of source/drain module fabrication with the best electrical properties, the partial relaxation phenomenon and the formation of defects must be avoided. It has been already proven in the literature that, for a given laser wavelength, reducing the pulse duration (i.e. increasing l/s interface propagation speed) should allow to circumvent the relaxation phenomenon [27-32]. With this in mind, we collaborated with C2N-CNRS to perform short pulse (25ns) laser annealing on our layers and compare the results.

4.4. Preliminary results on $\text{Si}_{0.7}\text{Ge}_{0.3}:\text{B}$ layers annealed by NLA (C2N)

4.4.1. Experimental details

The laser tool from C2N-CNRS has almost the same features as the tool from CEA-LETI (LT3100). They are both XeCl excimer lasers with a functioning wavelength of 308 nm. They differ in terms of pulse duration (25 ns (C2N) compared to 160 ns (LETI)), shot size ($2 \times 2 \text{ mm}^2$ compare $15 \times 15 \text{ mm}^2$) and environment conditions (the C2N laser is equipped with an ultra-high vacuum chamber while the LETI one works at atmosphere pressure). Nevertheless, for both laser tools, a beam homogeneity test is performed before each laser annealing process to confirm a $<2.0\%$ beam uniformity.

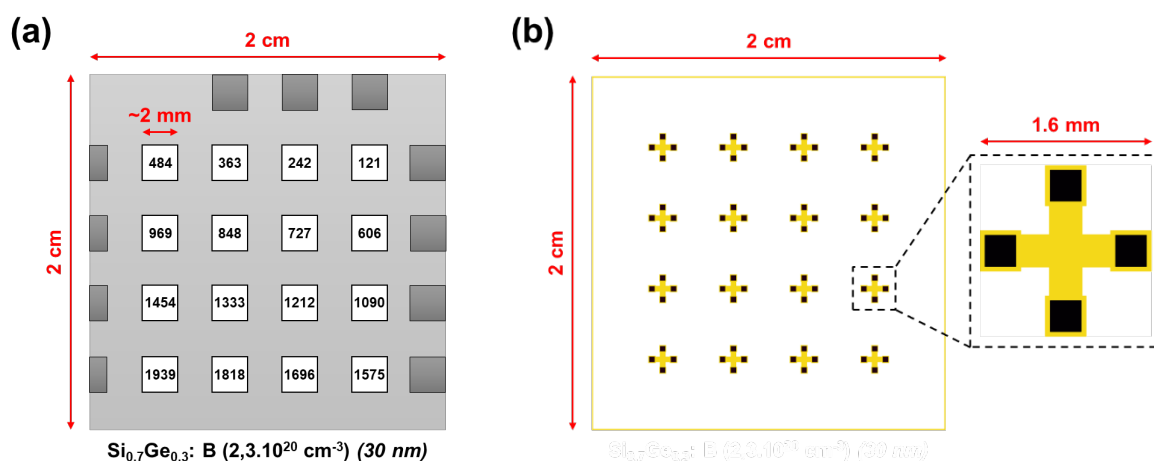


Figure 4.10: (a) Schematic of the laser annealing conditions performed on a $2 \times 2 \text{ cm}^2$ sample cut from the initial wafer corresponding to layer C (highly boron-doped strained- $\text{Si}_{0.7}\text{Ge}_{0.3}$ layer). (b) Mask layout for Van der Pauw cross-shaped structure fabrication associated to C2N laser annealing design of experiment.

For this experiment, we used $2 \times 2 \text{ cm}^2$ samples from layers A and C, which have the most distinctive electrical properties and from an undoped 45 nm thick $\text{Si}_{0.7}\text{Ge}_{0.3}$ layer. A single-pulse laser conditions series have been performed with energy densities between 121 and 1939 mJ/cm^2 , as schematised in **Fig. 4.10(a-c)**, for a total of 14 to 16 laser shots. A new set of masks has been designed to enable Hall measurements on the small irradiated areas (**Fig. 4.10(d)**). The associated fabrication process is divided in three steps: first, the structure etching (yellow layout), then, the metal (aluminium) deposition for structure contacts and finally, low temperature furnace annealing for contact optimisation (300°C , 2h). In addition, to facilitate the fabrication of the Van der Pauw structures, laser edge marks in melt conditions have been patterned to discern the sample orientation and to facilitate the alignment during the photolithography process (dark grey areas in **Fig. 4.10(a)**).

4.4.2. Preliminary discussion on electrical measurements

Sheet resistance measurements have been performed on the samples annealed with the C2N laser (see filled circle dots in **Fig. 4.11**) and compared to the measurements from the samples annealed by the CEA laser (filled diamond dots and triangle dots in **Fig. 4.11**). As both lasers do not have the sample pulse durations, an energy density rescaling was made on both horizontal axes until the sheet resistance profiles would coincide. When considering identical reference samples, we can notice that for a range of energy density values between

0.1 and 1.9 J/cm² for the C2N laser, higher values of energy densities must be used with the LETI laser to transmit the same thermal energy (between 1.0 – 2.9 J/cm²). This is consistent with the fact that the C2N laser (25 ns) is more powerful than the LETI laser (160 ns) for a given energy density. In addition, based on this hypothesis, we can deduce the laser regime transitions for the C2N samples by comparison with previous analysis made on LETI laser anneals (**part 4.2.1**). The laser regimes extracted from previous sections are shown in **Fig. 4.11** to illustrate the possible laser regime transitions existing in the C2N samples.

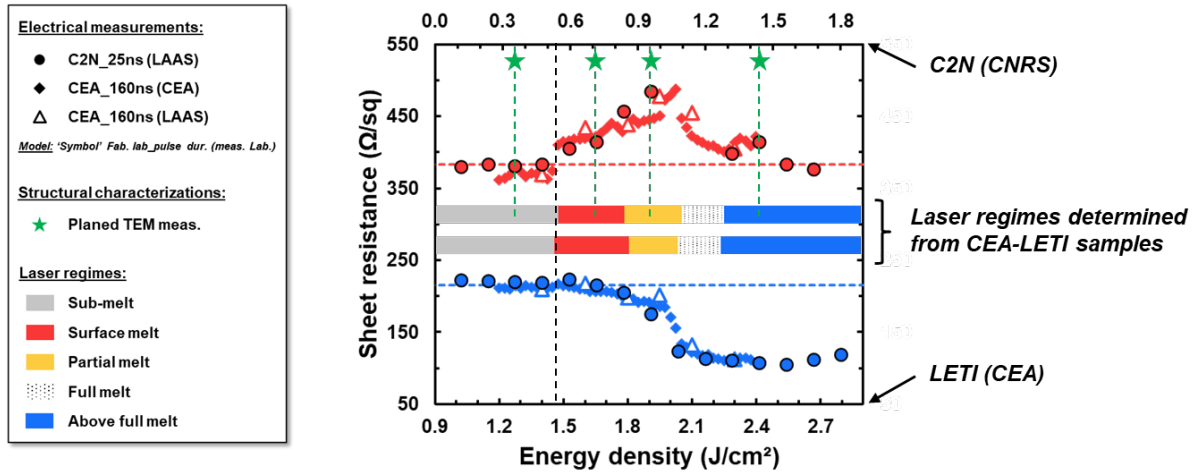


Figure 4.11: Sheet resistance evolution as function of the energy density for a lowly (A) and highly (C) boron-doped strained-Si_{0.7}Ge_{0.3} layers annealed by two laser tools with different pulse durations: CEA-LETI (160 ns) and CNRS-C2N (25 ns). Sheet resistance profiles from each laser has a dedicated energy density horizontal axis, the top one for C2N and the bottom one for LETI. Also, the laser regimes previously determined from our study on LETI samples are reported.

In haze measurements (see **Fig. 4.2(b)**), it has been observed that the transition from the sub-melt to the surface melt regime is characterized by an abrupt increase of the surface roughness. SEM and AFM images clearly show a surface morphology composed of melted islands that tend to increase in number at first and then in size. When reaching the partial melt regime, a continuous melted layer is formed, thus leading to a steep reduction of the surface roughness. To avoid any carbon contamination in boron-doped SiGe layers, we observed the surface of the undoped SiGe layer by SEM to find the distinctive sub-melt to surface melt transition. As shown in **Fig. 4.12(a)**, no surface asperities were discerned at 0.363 J/cm² (30 mV), in opposition to 0.484 J/cm² (40 mV), where the well-known surface morphology of laser annealed Si and/or SiGe layers can be found. The surface roughness can be used as a criterion to define a normalized reflectivity threshold for the sub-melt to surface melt transition detection in the TRR signals (dashed red line in **Fig. 4.12(a)**). By reporting this criterion to the TRR signals collected from laser anneals on boron-doped SiGe layers (**Fig. 4.12(b-c)**), it suggests that the previously discussed transition occurs at a higher energy density, between 0.484 and 0.606 J/cm². Interestingly, this also corresponds to the hypothesis made based on the CEA results in **Fig. 4.11** (see blacked dashed line). These assumptions will be experimentally verified using planed TEM cross-section observations on FIB lamella prepared from layer A samples annealed at 0.363, 0.727, 0.969 and 1.454 J/cm², that should correspond to sub-melt, surface melt, partial melt and above full melt regimes, respectively (green stars on dashed lines in **Fig. 4.11**).

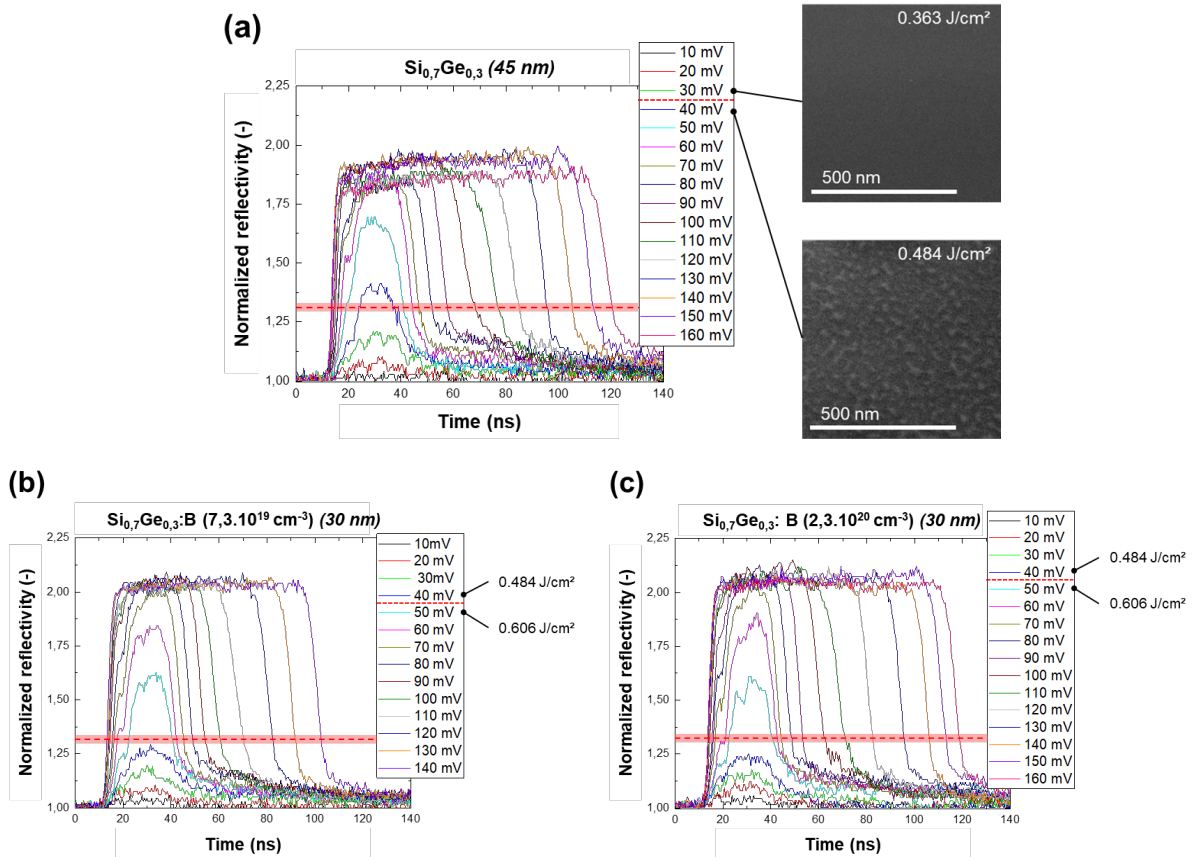
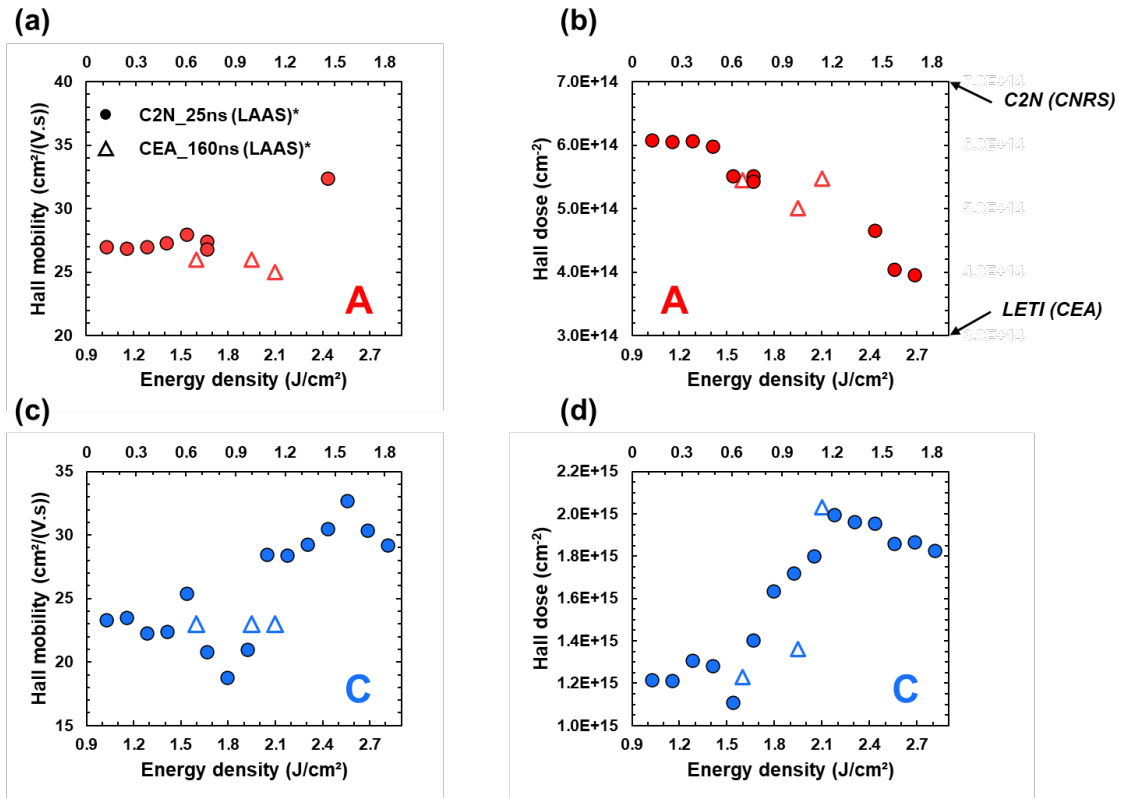


Figure 4.12: TRR curves from layers A (a), B (b) and C (c) annealed by CNRS-C2N laser tool at different energy densities (or voltage). For layer A, TRR curves are supported by SEM images of the surface at 0.363 and 0.484 J/cm². Red dashed lines for the three layers represent the normalized reflectivity threshold detection corresponding the beginning of the melt (surface melt).

SIMS profiles for all these samples are not yet available so we cannot evaluate their activation rates. However, it is possible to compare the raw data collected from Hall effect measurements for both different lasers (**Fig. 4.13(a-d)**). For each layer, the Hall mobilities and doses are in the same range of values suggesting the same involved behaviours upon laser annealing, independently of the pulse duration. Even if more data are required for a final conclusion, this preliminary study strongly suggest that short pulse duration laser annealing does not allow to circumvent the partial relaxation phenomenon (accompanied with the formation of defects).



*Legend caption: 'Symbol' Fabrication lab_pulse duration (measurement lab.)

Figure 4.13: Hall mobility (a,c) and dose (b,d) as function of the energy density measured by Hall effect for a lowly (A) and highly (C) boron-doped strained-Si_{0.7}Ge_{0.3} layers annealed by two laser tools with different pulse durations: CEA-LETI (160 ns) and CNRS-C2N (25 ns). All parameters measured depending on the laser tool have a dedicated energy density horizontal axis: the top one for C2N and the bottom one for LETI.

4.5. Key information

Key information – Dopant activation in laser annealed strained SiGe layers	
4.1.1	Characteristics of strained $\text{Si}_{0.7}\text{Ge}_{0.3}\text{:B}$: <ul style="list-style-type: none"> Fabricated by Reduced Pressure Chemical Vapor Deposition (RPCVD) and incorporated with Boron at 3 different concentrations: $7.3 \times 10^{19} \text{ cm}^{-3}$, $1.3 \times 10^{20} \text{ cm}^{-3}$ and $2.3 \times 10^{20} \text{ cm}^{-3}$ Annealed by LT3100 laser tool from SCREEN-LASSE (308 nm, 160 ns pulse duration, 3% non-uniformity, N_2 flow environment, 15x15 mm² irradiated zones)
4.1.2	Characterization methods: <ul style="list-style-type: none"> Electrical: 4-point probe and Hall effect Chemical: SIMS and TEM-EDX Structural: TRR, TEM (HR and weak beam), HR-XRD RSM and haze
4.1.3	Evaluation of the activation rate using a SIMS-Hall effect based algorithm: <ul style="list-style-type: none"> Objective: Match between calculated and measured Hall parameters Inputs: B and Ge SIMS profiles, Hall effect measurements and $r_H = f(x_{Ge})$ Extracted parameters: Maximum electrical concentration (C_{elec}), transport degradation factor (α) and activation rate (Ω)
4.2.1	Laser regimes identification: <ul style="list-style-type: none"> Determined by HR-TEM, TRR and haze 5 distinct regimes, not impacted by the amount of incorporated Boron: sub-melt, surface melt, partial melt, full melt and above full melt (order of apparition)
4.2.2	Strain state evaluation: <ul style="list-style-type: none"> Determined by HR-XRD RSM and TEM (weak beam) Partial relaxation appears during surface and partial melt regimes due to defect formation during recrystallization Compressive strain is preserved during sub-melt and recovered around full melt regimes
4.2.3	The specific case of strain recovery depends on the concentration of Boron (delayed for lowest doping layers) which is related to the stored elastic energy and does not necessarily match with the full melt regime
4.3.1	Study of as-grown s- $\text{Si}_{0.7}\text{Ge}_{0.3}\text{:B}$ layers: <ul style="list-style-type: none"> Activation rates of: ~100%, ~80% and ~60% No transport degradation ($\alpha \sim 1$), confirmed with $\mu(T)$ curves
4.3.2	In-depth analysis of R_S variations with ED, using Savitzky-Golay algorithm, for laser regimes and strain state identification: <ul style="list-style-type: none"> Refined identification of the laser regime ED threshold (compare to 4.2.1) More precise strain recovery transition evaluation than 4.2.2
4.3.3	Activation rates calculation in laser-annealed s- $\text{Si}_{0.7}\text{Ge}_{0.3}\text{:B}$ layers: <ul style="list-style-type: none"> Sub-melt, full melt and above: <ul style="list-style-type: none"> Initial compressive strain is preserved/recovered 100% activation is reached at full melt for all layers Surface melt and partial melt: <ul style="list-style-type: none"> Partial relaxation occurs and modifies material properties (through r_H) When taking "new" r_H into account, activation increases monotonically with ED (no deactivation phenomenon)
4.4.1	To possibly avoid partial relaxation due to NLA: <ul style="list-style-type: none"> New design of experiments with a short-pulse laser tool (25 ns) at C2N (CNRS) New Van der Pauw-Hall mask for 2x2 mm² laser shots
4.4.2	Preliminary results of laser-annealed s- $\text{Si}_{0.7}\text{Ge}_{0.3}\text{:B}$ layers with C2N laser: <ul style="list-style-type: none"> For data comparison between long-pulse and short-pulse laser, ED rescaling was made empirically Measured Hall parameters fits with LT3100 results which strongly suggest that partial relaxation occurs with short-pulse duration laser anneals Final TEM analyses are required to confirm our conclusions

Conclusion

In this deliverable, we have assessed the different questions raised in the previous deliverables, concerning the evolution of the liquid/solid interface roughness and also the correlation between structural and electrical properties when applying nanosecond laser annealing (D4.3). In addition, we have described in detail the fabrication process optimization related to the study on the impact of NLA on patterned nanostructures proposed in D4.2 and D4.4.

The experiments have shown that, when considering s-SiGe layers, the liquid/solid interface roughness generated in the melt regimes strongly depends not only on the germanium content but also on the strain state of the layer, which are both coupled. Indeed, to match the Si lattice parameter, SiGe layers need to be necessarily compressively strained (here biaxially). The stored elastic energy increases with the Ge content, and the required conditions to form a strained recrystallized layer are hard to fulfil. Adding boron dopants lowers the required energy density, giving the possibility to recover the strained and defects-free layers more easily than without dopants. To measure the impact of initial strain, undoped r-SiGe layers were studied at different Ge content. It has been shown that liquid/solid interface roughness still exists and is amplified when increasing the Ge content. Also, for a given energy density, it has been observed that the melt depth increases with Ge content. A possible lead would be that the liquid/solid interface roughness is decided at the early stage of the surface melt regime. This last hypothesis will be confirmed by cross-section TEM measurements.

Relaxed SiGe layers annealed by laser were further studied in terms of surface structuration, Ge redistribution and defects. In comparison to s-SiGe layers, very similar behaviours are found in terms of laser regimes. However, no crystal defects were observable despite a significant liquid/solid interface roughness. Also, the reached maximum Ge content close to the surface increases slowly when increasing the energy density. Pushing laser annealing conditions forward in the melt regimes exhibited unusual surface structuration and Ge redistributions from well-known standards. Indeed, supposedly due to interface solid roughness, recrystallization leads to the formation of almost pure Ge and homogeneously distributed buried walls. In addition, the surface morphology is strongly impacted and shows a square-grid pattern, the line being defined by Ge-rich walls and the centres by a r-SiGe crystal.

With a view to understanding the thermal phenomenon occurring in patterned SiGe nanostructures, it is mandatory to compare the current simulation models to experimental data. The third section of this deliverable was devoted to the fabrication process of such SiGe structures, meant to be annealed by laser. We have first presented the optimized fabrication process for the e-beam lithography and highly anisotropic vertical reactive ion etching applicable to any SiGe substrate. Secondly, using the same e-beam lithography technique, a sample layout of dense HSQ nanolines with different geometries has been realized on $\text{Si}_{0.8}\text{Ge}_{0.2}$ and $\text{Si}_{0.5}\text{Ge}_{0.5}$. These samples will soon be available for the laser anneal studies to be included in deliverable D4.7 in comparison to the simulation results of the here presented nanoline arrays.

In the last section, we studied in detail the electrical properties of boron-doped s-SiGe at different levels of concentration. Based on the results presented in D4.3, the laser regime transitions and strain state evolution were summarized to display a global view of the crystal structure as function of the laser energy density. Thanks to sheet resistance profiles as function of the energy density, it was possible to perfect our understanding of the laser regime and strain state transitions. An algorithm comparing Hall measurements and calculated Hall values from Ge and B SIMS profiles has been developed to extract three parameters: the electrical concentration level, the transport degradation factor and the activation rate. After several

recalibration and optimization steps made using SIMS profiles, this analysis method allowed us to understand more precisely the electrical properties of the as-grown s-SiGe:B layers (refined analysis compared to D3.3) and the laser-annealed layers (extended analysis from D4.3). From partially to almost fully activated layers, and considering the structural and strain properties, the results confirmed that NLA in melt condition necessarily improves the activation monotonically with increasing energy density. For device fabrication purposes, it was proposed to use short-pulse duration laser annealing to avoid the formation of defects, leading to partial relaxation. Laser anneals with an identical wavelength (308 nm) tool but with a pulse duration of 25 ns instead of 160 ns were performed on the studied layers. Preliminary results strongly suggest that reducing the pulse duration does not avoid defect formation though further investigations are required to corroborate this conclusion.

References

- [1] L. Dagault et al., "Investigation of recrystallization and stress relaxation in nanosecond laser annealed $\text{Si}_{1-x}\text{Ge}_x/\text{Si}$ epilayers", *Applied Surface Science*, **527**, 146752, 2020.
- [2] P.I. Gaiduk & S. L. Prakopyeu, "Structural changes in SiGe/Si layers induced by fast crystallization", in: Skorupa, W, Schmidt, H. (eds) *Subsecond Annealing of advanced materials*. Springer Series in Materials Science, **192**. Springer, Cham.
- [3] N. A. Sobolev et al., "Pulsed laser annealing of Si-Ge superlattices", *Materials Science and Engineering C*, **23**, 19-22, 2003.
- [4] T. Tabata et al., "Segregation and activation of Ga in high Ge content SiGe by UV melt laser anneal", *J. Appl. Phys.*, **125**, 215702, 2019.
- [5] R. Gotoh et al., "Formation mechanism of cellular structures during unidirectional growth of binary semiconductor Si-rich SiGe materials", *Appl. Phys. Lett.*, **100**, 021903, 2012.
- [6] G. Larrieu, Y. Guerfi, X.-L. Han and N. Clément, "Sub-15 nm gate-all-around field effect transistors on vertical silicon nanowires", *Solide-State Electronics*, **130**, 9-14, 2017.
- [7] Y. Guerfi, F. Carcenac and G. Larrieu, "High resolution HSQ nanopillar arrays with low energy electron beam lithography", *Microelectron. Eng.*, **110**, 173-176, 2013.
- [8] G. S. Oehrlein, G. M. W. Kroesen, E. de Frésart, Y. Zhang, and T. D. Bestwick, "Studies of the reactive ion etching of SiGe alloys", *J. Vac. Sci. Technol. A*, **9** (3), 768-774, 1990.
- [9] G. S. Oehrlein, Y. Zhang, G. M. W. Kroesen, E. de Frésart, and T. D. Bestwick, "Interactive effects in the reactive ion etching of SiGe alloys", *Appl. Phys. Lett.*, **58** (20), 2252-2254, 1991.
- [10] Y. Ishii, R. Scott-McCabe, A. Yu, K. Okuma, K. Maeda, J. Sebastian and J. Manos, *Jpn. J. Appl. Phys.* **57**, 6JC04, 2018.
- [11] G. S. Oehrlein, G. M. W. Kroesen, and J. L. Lindström, "Etching of silicon in low-pressure plasmas containing fluorine and oxygen: A comparison of real-time and postplasma surface studies", *J. Vac. Sci. Technol. A*, **10** (5), 3092-3099, 1992.
- [12] R. Daubriac, "Caractérisation de techniques d'implantations ioniques alternatives pour l'optimisation du module source-drain de la technologie FDSOI 28nm", Ph. D. thesis, 2018.
- [13] J. M. McGregor, T. Manku, J.-P. Noël, D. J. Roulston, A. Nathan and D. C. Houghton, "Measured In-Plane Hole Drift and Hall Mobility in Heavily-Doped Strained p-type $\text{Si}_{1-x}\text{Ge}_x$ ", *Journal of Electronic Materials*, **22** (3), 319-321, 1993.
- [14] T. K. Carns, S. K. Chun, M. O. Tanner, K. L. Wang, T. I. Kamins, J. E. Turner, D. Y. C. Lie, M.-A. Nicolet and R. G. Wilson, "Hole Mobility Measurements in Heavily Doped $\text{Si}_{1-x}\text{Ge}_x$ Strained Layers", *IEEE Transactions on Electron Devices*, **41** (7), 1273-1281, 1994.
- [15] Y. C. Chen, S. H. Li, P. K. Bhattacharya, J. Singh, and J. M. Hinckley, "Direct measurement of the Hall factor for holes in relaxed $\text{Si}_{1-x}\text{Ge}_x$ ", *Applied Physics Letters*, **64**, 3110-3111, 1994.
- [16] Y. Fu, K. B. Joelsson, K. J. Grahn, W.-X. Ni, G. V. Hansson and M. Willander, "Hall factor in strained p-type doped $\text{Si}_{1-x}\text{Ge}_x$ alloy", *Physical Review B*, **54** (16), 11317-11321, 1996.

- [17] K. B. Joelsson, Y. Fu, W.-X. Ni and G. V. Hansson, "Hall factor and drift mobility for hole transport in strained $\text{Si}_{1-x}\text{Ge}_x$ alloys", *Journal of Applied Physics*, **81**, 1264-1269, 1997.
- [18] J. E. Dijkstra and W. Th. Wenckebach, "Effects of strain and alloying on the Hall scattering factor for holes in Si and $\text{Si}_{1-x}\text{Ge}_x$ ", *Journal of Applied Physics*, **85**, 1587-1590, 1999.
- [19] R. J. P. Lander, Y. V. Ponomarev, J. G. M. van Berkum, W. B. de Boer, R. Loo and M. Caymax, "Drift mobilities and Hall scattering factors of holes in ultrathin $\text{Si}_{1-x}\text{Ge}_x$ layers ($0.3 < x < 0.4$) grown on Si", *Journal of Applied Physics*, **88** (4), 2016-2023, 2000.
- [20] P. Kinsler and W. Th. Wenckebach, "Hall effect and ionized impurity scattering in $\text{Si}_{1-x}\text{Ge}_x$ ", *Journal of Applied Physics*, **94** (11), 7159-7162, 2003.
- [21] L. Dagault, "Etude du comportement de couches $\text{Si}_{1-x}\text{Ge}_x$ soumises au recuit laser nanoseconde ultraviolet », Ph. D. Thesis, 2021.
- [22] S. K. Chun and K. L. Wang, "Effective Mass and Mobility of Holes in Strained $\text{Si}_{1-x}\text{Ge}_x$ Layers on (001) Si_{1-y}Ge_y Substrate", *IEEE Transactions on Electron Devices*, **39** (9), 2153-2164, 1992.
- [23] O. Weber; T. Irisawa; T. Numata; M. Harada; N. Taoka; Y. Yamashita; T. Yamamoto; N. Sugiyama; M. Takenaka; S. Takagi, "Examination of Additive Mobility Enhancements for Uniaxial Stress Combined with Biaxially Strained Si, Biaxially Strained SiGe and Ge Channel MOSFETs", *International Electron Devices Meeting*, 10-12 December, Washington DC USA, 2007.
- [24] L. Gomez, P. Hashemi and J. L. Hoyt, "Enhanced Hole Transport in Short-Channel Strained-SiGe p-MOSFETs", *IEEE Transactions on Electron Devices*, **56** (11), 2644-2651, 2009.
- [25] P. Acosta Alba, S. Kerdilès, B. Mathieu, R. Kachtouli, P. Besson, M. Veillerot, F. Aussenac, C. Fenouillet-Béranger, F. Mazzamuto, I. Toqué-Trésonne and K. Huet, "Nanosecond laser annealing for phosphorous activation in ultra-thin implanted Silicon-On-Insulator substrates", *21st International Conference on Ion Implantation Technology (IIT)*, 26-30 September, Tainan, Taiwan, 2016.
- [26] G. V. Luong, S. Wirths, S. Stefanov, B. Holländer, J. Schubert, J. C. Conde, T. Stoica, U. Breuer, S. Chiussi, M. Goryll, D. Buca, and S. Mantl, "Study of dopant activation in biaxially compressively strained SiGe layers using excimer laser annealing", *Journal of Applied Physics*, **113**, 204902, 2013.
- [27] P. Baeri, J. M. Poate, S. U. Campisano, G. Foti, E. Rimini, and A. G. Cullis, "Dependence of trapping and segregation of indium in silicon on the velocity of the liquid/solid interface", *Applied Physics Letters*, **37**, 912-914, 1980.
- [28] J. J. P. Bruines, R. P. M. van Hal, H. M. J. Boots, A. Polman, and F. W. Saris, "Time resolved reflectivity measurements during explosive crystallization of amorphous silicon", *Appl. Phys. Lett.*, **49**, 1160-1162, 1986.
- [29] J. J. P. Bruines, R. P. M. van Hal, H. M. J. Boots, W. Sinke, and F. W. Saris, "Direct observation of resolidification from the surface upon pulsed laser melting of amorphous silicon", *Applied Physics Letters*, **48**, 1252-1254, 1986.

[30] D. P. Brunco, M. O. Thompson, D. E. Hoglund, M. J. Aziz and H.-J. Gossmann, "Germanium partitioning in silicon during rapid solidification", *Journal of Applied Physics*, **73** (3), 1575-1582, 1995.

[31] C. Y. Ong, K. L. Pey, X. Li, X. C. Wang, C. M. Ng et al., "Laser annealing induced high Ge concentration epitaxial SiGe layer in Si_{1-x}Ge_x virtual substrate", *Appl. Phys. Lett.*, **93**, 041112, 2008.

[32] C. Y. Ong, K. L. Pey, K. K. Ong, D. X. M. Tan, X. C. Wang, H. Y. Zheng, C. M. Ng, and L. Chan, "A low-cost method of forming epitaxy SiGe on Si substrate by laser annealing", *Applied Physics Letters*, **94**, 082104, 2009.